

1 **This manuscript is a preprint** and has been submitted for publication in Journal of
2 Volcanology and Geothermal Research. Please note that, the manuscript is currently under
3 review and has yet to be formally accepted for publication. Subsequent versions of this
4 manuscript may have different content. If accepted, the final version of this manuscript will
5 be available via the 'Peer-reviewed Publication DOI' link on the right-hand side of this
6 webpage. Please feel free to contact me with any comments or feedback on our study.

7
8
9
10
11
12
13
14
15
16
17
18
19
20
21
22
23
24
25
26
27
28
29
30
31
32
33
34
35
36
37
38
39
40
41
42
43
44

45 **AMS and rock magnetism in the Caviahue-Copahue Volcanic Complex**
46 **(Southern Andes): emission center, flow dynamics, and implications to the**
47 **emplacement of non-welded PDCs**

48
49 *Mauricio Barcelos Haag^{a,*}, Carlos Augusto Sommer^a, Jairo Francisco Savian^a, Alberto Tomás Caselli^b,*
50 *Thiago Ribas Moncinhatto^c, Gelvam André Hartmann^d, Michael H Ort^e, Wilbor Poletti^f,*
51 *Ricardo Ivan Ferreira da Trindade^c*

52
53 ^a*Instituto de Geociências, Universidade Federal do Rio Grande do Sul, Av. Bento Gonçalves 9500, 91501-970*
54 *Porto Alegre, RS, Brazil*

55 ^b*Laboratorio de Estudio y Seguimiento de Volcanes Activos, Universidad Nacional de Río Negro, Roca 1242,*
56 *8332 G. Roca, Rio Negro, Argentina*

57 ^c*Instituto de Astronomia, Geofísica e Ciências Atmosféricas, Universidade de São Paulo, Rua do Matão 1226,*
58 *05508-090 São Paulo, SP, Brazil*

59 ^d*Instituto de Geociências, Universidade Estadual de Campinas, Rua Carlos Gomes 250, 13083-855 Campinas,*
60 *SP, Brazil*

61 ^e*School of Earth and Sustainability, Box 4099, Northern Arizona University, Flagstaff, AZ, 86011 USA*

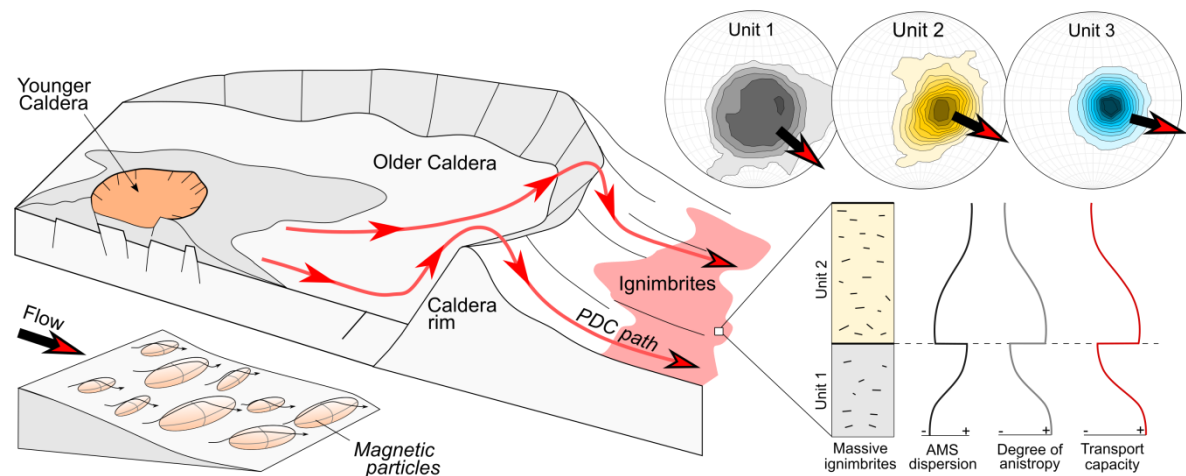
62 ^f*Instituto de Ciência e Tecnologia, Universidade Federal dos Vales do Jequitinhonha e Mucuri, Rodovia MGT-*
63 *367, 5000, 39100-000 Diamantina, MG, Brazil*

64 * Corresponding author: M.B. Haag

65 E-mail address: mauricio.haag@ufrgs.br / mauricio.barceloshaag@gmail.com

66 Twitter account: @haag_mauricio

67
68
69 **Graphical abstract**



73 Abstract

74 Pyroclastic deposits can cover significant areas and register major geological events. Despite
75 their importance, understanding depositional dynamics of pyroclastic density currents (PDCs)
76 and linking explosive deposits to their emission centers is still a challenge, especially in the
77 case of non-welded, massive ignimbrites. Located in the Southern Andes, the Caviahue
78 Copahue Volcanic Complex (CCVC) comprises one of the most active volcanic centers in the
79 Andean Belt. This volcanic complex hosts massive ignimbrites with both source emplacement
80 poorly constrained, currently grouped in the Riscos Bayos Ignimbrites (RBI). In this
81 contribution, we perform a full magnetic characterization and anisotropy of magnetic
82 susceptibility (AMS) study on the massive RBI of the CCVC. The magnetic characterization
83 was performed using magnetic experiments including isothermal remanent magnetization,
84 thermomagnetic curves, hysteresis loops, first-order reversal curves, and scanning electron
85 microscopy. Magnetic experiments indicate primary, multi-domain, high Curie temperature
86 titanomagnetites as the AMS carriers. Ellipsoids are predominately oblate, with a low degree
87 of anisotropy and east-southeastward imbrication. This fabric arrangement is consistent with
88 PDC sedimentary fabrics deposited under laminar flow conditions. Despite RBI massive
89 structure AMS data reveals changes in transport capacity of the PDC and particle
90 organization. These changes are marked by increasing AMS dispersion and decreasing degree
91 of anisotropy up-section within flow units. Directional statistics of AMS data implies the Las
92 Mellizas Caldera as the emission center of RBI. The reconstructed flow path also suggests the
93 PDC overrun of the Caviahue Caldera topographic rim. This study highlights the application
94 of AMS to the identification of emission centers of explosive deposits, featuring its
95 application to massive ignimbrites.

96

97 **Keywords:** Magnetic fabrics; Magnetic mineralogy; AMS; Pyroclastic density current; Non-
98 welded ignimbrite; Andes

99 1. Introduction

100 Pyroclastic density currents (PDCs) are the main products of explosive volcanism and
101 produce a wide variety of deposits, including welded to non-welded ignimbrites (Sparks,
102 1976; Cas and Wright, 1987). These explosive deposits can cover extensive areas and record a
103 significant portion of the geological history, as documented in the Snake River and
104 Yellowstone Volcanic Province (USA; Morgan et al., 1984), Sierra Madre Occidental
105 (Mexico; Ferrari et al., 2002), and the Altiplano-Puna Volcanic Complex (Argentina and
106 Chile; de Silva, 1989; Lesti et al., 2011). Despite their geological significance, linking
107 explosive deposits to their source areas and understanding depositional processes in PDCs is
108 still a challenge, with several unresolved emission centers around the world (e.g., Morgan et
109 al., 1984; Giordano et al., 2008; Agrò et al., 2014) and in the Andean Belt (e.g., Lesti et al.,
110 2011; Ort et al., 2014; Platzmann et al., 2020). This happens because, in active regions
111 tectonics and climate can rapidly modify volcanic landscapes, preferentially removing non-
112 welded deposits. As a consequence, the study of PDC deposits in these environments
113 demands the application of alternative techniques. The anisotropy of magnetic susceptibility
114 (AMS) is helpful to understand the mechanisms and flow dynamics of pyroclastic flow
115 deposits.

116 AMS estimates the orientation of the magnetic particles of a given rock sample,
117 detecting a rock fabric that can be used to study paleocurrent, deformation, and rheological
118 processes in all kinds of rocks (Graham, 1954; Hrouda, 1982; Cañón-Tapia and Mendoza-
119 Borunda, 2014). AMS studies have been applied to volcanic rocks, allowing the
120 determination of source area, transport, and emplacement conditions of PDCs (e.g., Palmer
121 and MacDonald, 1999; Ort et al., 2003; LaBerge et al., 2009; Cas et al., 2011; Cañón-Tapia
122 and Mendoza-Borunda, 2014; Ort et al., 2014), lavas (e.g., Cañón-Tapia et al., 1997; Benites
123 et al., 2020; Pasqualon et al., 2020, Haag et al., 2021) and dikes and sills (e.g., Magee et al.,

124 2012). Nevertheless, how PDC processes are recorded in magnetic fabrics is still debated
125 because many factors can influence the petrofabrics to produce a variety of AMS fabrics (e.g.,
126 Ort et al., 2014; Cañón-Tapia and Mendoza-Borunda, 2014). The presence of extensive
127 ignimbrite deposits in the Cavihue-Copahue Volcanic Complex (CCVC) in northern
128 Patagonia provides a key area for the study of AMS fabrics in ignimbrites.

129 Located in the southern Andes (between Argentina and Chile), the CCVC (Fig. 1)
130 comprises one of the most active volcanic centers in this orogenic segment (Caselli et al.,
131 2016; Tassi et al., 2016). Despite the young age (< 5 Ma, Linares et al., 1999), CCVC
132 deposits were strongly affected by Pleistocene glaciations (Díaz, 2003; Varekamp et al., 2006;
133 Báez et al., 2020a), leading to a fragmented record and establishing a geologic puzzle,
134 especially in the case of the more friable, volcanoclastic deposits. As a result, the explosive
135 deposits in the CCVC provide an excellent case for the study of AMS fabrics in non-welded
136 ignimbrites. The Riscos Bayos Ignimbrites (RBI), located a few kilometers outside the
137 southern border of the Cavihue Caldera (Melnick et al., 2006), consist of a sequence of
138 predominantly non-welded ignimbrites with restricted outcrops (Mazzoni and Licitra, 2000;
139 Varekamp et al., 2006). This unique low-grade ignimbrite sequence (RBI) in the region is a
140 significant geologic unit for the understanding of the CCVC (Mazzoni and Licitra, 2000), as
141 well as a case study for the determination of emission centers of large-volume, non-welded
142 PDCs deposits.

143 This work constrains the emplacement conditions and the source area of RBI,
144 exploring its relations with the CCVC. We conducted fieldwork at the CCVC and performed
145 a systematic sampling for AMS analyses and full magnetic mineralogy characterization. This
146 approach allowed us to determine the flow direction of the RBI PDCs and link the AMS with
147 flow dynamics of these flows. Our data suggest a decrease in transport capacity toward the
148 top of each flow unit, marked by an increase in AMS dispersion and a decrease in the degree

149 of anisotropy. Directional analysis indicates the Las Mellizas Caldera as the emission center
150 for the RBI.

151

152 **2. Geological setting**

153 Located in the Southern Volcanic Zone (SVZ) of the Andes (Fig. 1), the CCVC
154 ($37^{\circ}50'S$, $71^{\circ}10'W$) comprises a singular volcanic center composed of the active
155 stratovolcano Copahue (1.23 Ma – Recent) and the Pliocene Caviahue (also known as *Agrio*)
156 Caldera (Pesce, 1989; Melnick et al., 2006; Fig. 1). In the SVZ, the magmatic activity occurs
157 as a result of the subduction of the Nazca Plate under the South American Plate, with
158 extensive volcanism of basaltic to andesitic composition (Hildreth and Moorbath, 1988; Stern,
159 2004). In this context, the CCVC composes one of the most active volcanic centers in the
160 Andean belt, with several eruptive events in the last century (Caselli et al., 2016; Tassi et al.,
161 2016). The particular setting of the CCVC attracted several studies in the recent decades, with
162 a broad range of topics including geomorphology (e.g., Díaz, 2003; Báez et al., 2020a),
163 geochemistry (e.g., Mazzoni and Licitra, 2000; Melnick et al., 2006; Varekamp et al., 2006),
164 geochronology (e.g., Pesce, 1989; Melnick et al., 2006) structural (e.g., Melnick et al., 2006;
165 Velez et al., 2011; Folguera et al., 2016), geothermal (e.g., Barcelona et al., 2019), and AMS
166 and paleomagnetism (e.g., Ort et al., 2014; Moncinhatto et al., 2019, 2020).

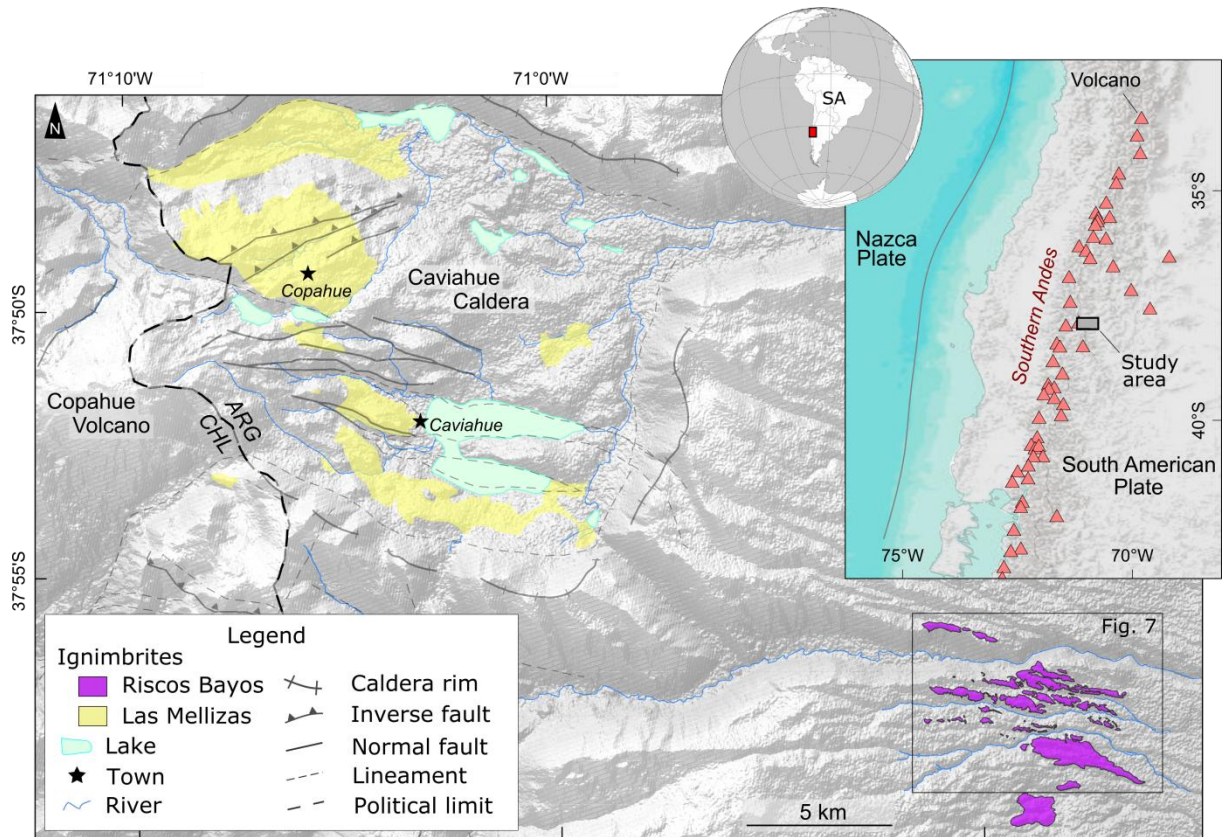
167 Both Copahue and Caviahue are controlled by a complex structural setting, with
168 significant influence of the oblique subduction of the Nazca Plate on caldera and volcano
169 edifice morphology (Melnick et al., 2006), as well as on vent location and spatial distribution
170 (Stern, 2004; Sielfeld et al., 2017). In addition to this active tectonic setting, several features
171 indicate a strong glacial imprint on CCVC deposits, including U-shaped valleys, striations in
172 lava flows, and moraine deposits (Díaz, 2003; Varekamp et al., 2006; Báez et al., 2020a). The
173 age and intensity of this glaciation are still unclear (Báez et al., 2020a).

174 The CCVC is marked by abundant effusive and explosive deposits (Melnick et al.,
175 2006), which extensively cover and partially fill the Caviahue Caldera. Related to Pleistocene
176 evolution, two main pyroclastic units are identified in the region (Mazzoni and Licitra, 2000):
177 the Las Mellizas Volcanic Sequence (LMVS, ~ 2.6 Ma; Linares et al., 1999), which occupies
178 the inner portion of the Caviahue Caldera, and the Riscos Bayos Ignimbrites (RBI, 2.0 - 1.1
179 Ma; Muñoz and Stern, 1988; Linares et al., 1999), which are prominently located about 15 km
180 southeast of the Caviahue Caldera but also cover ~ 100 km² on the top of the mesa to the east
181 of the caldera (Fig. 1). The LMVS is marked by strongly welded andesitic to dacitic
182 ignimbrites and rheoignimbrites containing abundant lithic fragments (Mazzoni and Licitra,
183 2000; Melnick et al., 2006; Sommer et al., 2016), interbedded with extensive lava flows
184 (Varekamp et al., 2006).

185 In contrast, the RBI forms irregular ENE-WSW-trending ridges (Fig. 1) in the Riscos
186 Bayos area and consists of a sequence of predominantly non-welded rhyolitic ignimbrites,
187 with an abundant ash matrix composed of pumice and lithic fragments of volcanic origin
188 (Mazzoni and Licitra, 2000; Melnick et al., 2006; Varekamp et al., 2006). On the mesa to the
189 east of the Caviahue caldera, the ignimbrite, up to ~100 m thick, is incipiently to moderately
190 welded and forms ENE-WSW-trending ridges. Additional mapping of RBI is still necessary
191 to determine the total extent of the deposits (Ort et al., 2014). The available data indicate
192 contrasting ages for RBI, caused either by analytical errors or contamination (Melnick et al.,
193 2006).

194 Both vent location and nature of the RBI are also poorly constrained. Some studies
195 have associated this ignimbrite sequence with the collapse of the Las Mellizas Caldera (Pesce,
196 1989; Melnick et al., 2006), a volcano originally located to the west of the Caviahue Caldera
197 where the Copahue Volcano is now located. Others associate RBI with Caviahue Caldera
198 collapse (Mazzoni and Licitra, 2000), while some authors have argued that RBI could not

199 account for the collapse based on volume estimates (Varekamp et al., 2006). These volume
 200 estimates, in contrast, are still debated (Ort et al., 2014).



201
 202 **Fig. 1.** Shaded relief map of the CCVC with the main ignimbrite deposits, geological features, and structures.
 203 ARG - Argentina; CHL - Chile. To the right: inset with the context of the studied area in the globe and in the
 204 Southern Andean Belt. SA - South America.

205
 206 **3. Methods**

207 *3.1. Fieldwork and paleomagnetic sampling*

208 RBI outcrops were first identified using Google Earth and available geological maps
 209 from the literature (e.g., Melnick et al., 2006). The best accessible RBI exposures occur 15 km
 210 SW of the southeastern rim of the Caviahue Caldera, along the Argentinian road number 26.
 211 A field evaluation regarding the main structures and primary constituents was performed in
 212 every outcrop, including compass measurements. For AMS studies, a total of 144 cores (25.4
 213 mm in diameter) were obtained from 10 sampling sites using a portable gasoline-powered

214 drill. The samples were oriented using a magnetic compass and whenever possible a sun
215 compass for corrections.

216

217 *3.2. Laboratory investigations*

218 *3.2.1. Microscopy*

219 Thin sections were prepared and analyzed under an optical microscope with
220 transmitted (for silicate fabrics) and reflected light (for Fe-Ti oxide fabrics). Using the
221 software ImageJ ([Schindelin et al., 2012](#)), the orientation of the major axis of both silicate and
222 oxide crystals of representative samples were extracted, allowing comparison and validation
223 of the directions obtained using the AMS technique.

224

225 *3.2.2. Rock magnetism*

226 To identify the magnetic carriers and the nature of the magnetism in RBI, we
227 characterized our samples using several experiments including temperature-dependent
228 magnetic susceptibility curves (χ -T), isothermal remanent magnetization (IRM) acquisition
229 curves, hysteresis loops, and first-order reversal curves (FORC). All magnetic measurements
230 were performed at the Paleomagnetism Laboratory of the University of São Paulo (USPMag).

231 One representative powdered sample from each site (total of 10 samples) was used to
232 determine the Curie temperature (T_c) and phase transitions and of the magnetic minerals using
233 temperature-dependent low-field magnetic susceptibility curves (χ -T diagrams). The samples
234 were heated from room temperature up to ~ 600 °C using a Kappabridge KLY4 coupled with
235 a CS3 furnace (AGICO). The results were corrected and analyzed using the software
236 Cureval8 (AGICO), where the T_c values were obtained by the second derivative of the
237 heating curve ([Tauxe, 2018](#)).

238 IRM curves and hysteresis loops were determined using small rock chips from each
239 site. Analyses were performed at room temperature using a Princeton Measurements
240 Corporation Micromag vibrating sample magnetometer (VSM) by applying fields up to 1 T.
241 From these analyses, we derived basic parameters, including the saturation magnetization
242 (M_s), saturation remanent magnetization (M_{rs}), coercivity (B_c), and coercivity of remanence
243 (B_{cr}). In order to model the magnetic components present in our samples, UnMix analyses
244 (Robertson and France, 1994; Kruiver et al., 2001; Heslop et al., 2002) were performed using
245 the IRM acquisition curves. Quantification and UnMix fitting were accomplished using the
246 MAX UnMix application (Maxbauer et al., 2016), with a smoothing factor of 0.5.

247 Hysteresis parameters are not sufficient for discriminating the different magnetic
248 components and structural states because they provide only a measurement of the sample bulk
249 properties (Roberts et al., 2018). Considering the complex magnetic mineralogy observed in
250 our samples (Moncinhatto et al., 2020), we obtained FORCs to better characterize our
251 magnetic assemblage. FORC diagrams (Roberts et al., 2000) were obtained at room
252 temperature after 300 reversal curves with an average time of 200 ms. The data were
253 processed using the FORCinel software package (Harrison and Feinberg, 2008), applying a
254 smoothing factor of 5 to all samples.

255 Further investigation of silicate and iron oxide composition was carried out using a
256 scanning electron microscope (SEM) model Jeol JSM 6610-LV operated at a beam voltage of
257 15kV, and energy-dispersive X-ray spectroscopy (EDS), at the Laboratory of Isotope Geology
258 of the Federal University of Rio Grande do Sul (LGI-UFRGS).

259

260 3.2.3. AMS analysis

261 In this work, we apply the AMS to interpret the petrofabrics of the studied ignimbrites
262 and determine the flow direction of the PDC. The AMS signal consists of a superposition of

263 diamagnetic, paramagnetic and ferromagnetic minerals, depending on their intrinsic
264 anisotropy and spatial distribution within a rock sample (Tarling and Hrouda, 1993). This
265 technique is based on the measurement of the magnetic susceptibility in different directions to
266 resolve the magnetic susceptibility tensor (K), which ultimately represents the shape and
267 orientation of the particles in the sample (represented by the principal axes $K_1 \geq K_2 \geq K_3$),
268 allowing several interpretations related to flow direction and regime in volcanic rocks
269 (Graham, 1954; Cañón-Tapia and Mendoza-Borunda, 2014).

270 In the laboratory, samples were cut into standard specimens (25.4 mm in diameter, 22
271 mm in thickness), totaling 144 specimens. AMS analyses were performed on standard
272 specimens from all sites, using an automatic Kappabridge MFK1-A apparatus (AGICO),
273 operated in a low alternating field of 300 A/m and a frequency of 976 Hz. Results were
274 processed and interpreted using Anisoft5 (AGICO), and later plotted in a geographic
275 information system (GIS) environment to aid the spatial interpretation. All the stereonet
276 presented are in the bedding coordinate system (bedding being rotated to the horizontal).

277 All AMS analyses were performed at the USPMag. To reach a more robust directional
278 analysis, we also reprocessed 13 paleomagnetic sites from Ort et al. (2014), who performed an
279 AMS and paleomagnetic analysis in the CCVC with a greater focus on AMS fabrics and their
280 behavior with respect to PDC deposition. In order to better constrain confidence intervals and
281 the principal AMS axes, bootstrap resampling was applied to our samples (Constable and
282 Tauxe, 1990; Tauxe et al., 1991).

283

284

285

286

287

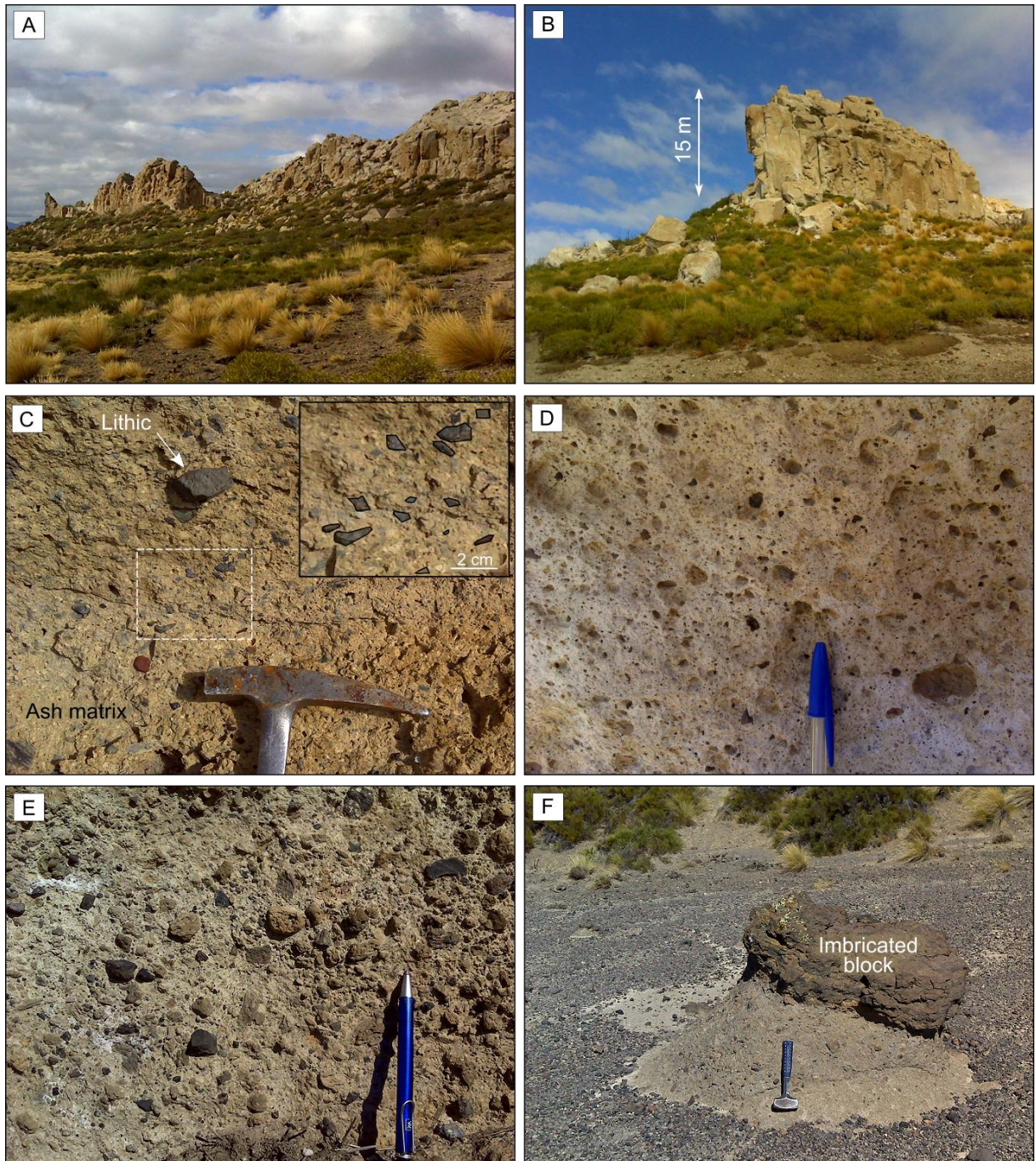
288 4. Results

289 4.1. Field and petrographic aspects

290 In the study area the RBI crops out as ENE-WSW-trending ridges marked by distinct
291 tan, white and grey colors (Fig. 2A). The northern section is dominated by tan and grey
292 irregular ridges stretching for up to ~ 3 km, while the southern section is composed of a white
293 ~ 4-km-long continuous ridge. Flow units are tabular, with thickness ranging from a few to 15
294 m (Fig. 2B). RBI samples are mainly poorly sorted lapilli-tuffs with 20 to 35% of ash, 65 to
295 75% of lapilli, and less than 2% of block fragments. The lapilli and block fragments are
296 mainly composed pumice (80 - 95%) fragments, with variable contents of lithic clasts (5 -
297 20%), mainly of andesite and basalt (Fig. 2C, D). Pumice, lithic and crystal are supported by a
298 fine matrix mainly composed of pumice and crystal fragments.

299 In some sites, the matrix and the clasts present a slight imbrication to the southeast
300 (Fig. 2C). Despite that, massive and graded bedding dominates as the main structures
301 observed in RBI. A normal grading for lithic clasts and an inverse grading for pumice clasts
302 are common, as well as pumice concentration zones. The upper section presents high primary
303 and secondary porosities and is marked by higher pumice contents (Fig. 2D). Pumice
304 fragments can reach up to 20 cm in diameter. In the basal section, thin horizons with a
305 concentration of lithic clasts are common (Fig. 2E), where lithic fragments can reach up to 30
306 cm in diameter. In several locations, a high variation in grain size and distribution occurs,
307 including the sparse presence of blocks and bombs (Fig. 2F).

308



309

310 **Fig. 2.** Field and petrographic aspects of RBI. A) ENE-WSW-trending ridges of RBI outcrops; B) outcrop of
311 tan-colored ignimbrite sequence; C) poorly-sorted lapilli-tuff with incipient imbrication (inset); D) upper section
312 pumiceous lapilli-tuff; E) lithic-rich basal section; F) block-sized imbricated fragment.

313

314 Under the microscope, RBI samples are marked by pumice, lithic, and crystal
315 fragments surrounded by fine ash matrix. The ash matrix is predominantly composed of
316 partially oxidized shards, as well as crystal fragments (Fig. 3A, B). Crystal, lithic and pumice

317 fragments are typically lapilli, with diameters ranging from 3 to 30 mm (Fig. 3A-D).
318 Petrographic compositional estimations of RBI main body (Fig. 3C) reveal a predominance of
319 pumice fragments (66 - 90%), followed by crystal (4 - 9%) and lithic fragments (1 - 3%).
320 Pumices dominate the lapilli and ash size intervals, while crystals tend to concentrate within
321 the ash fraction (Fig. 3C). The amount of matrix ranges from 15 to 40%.

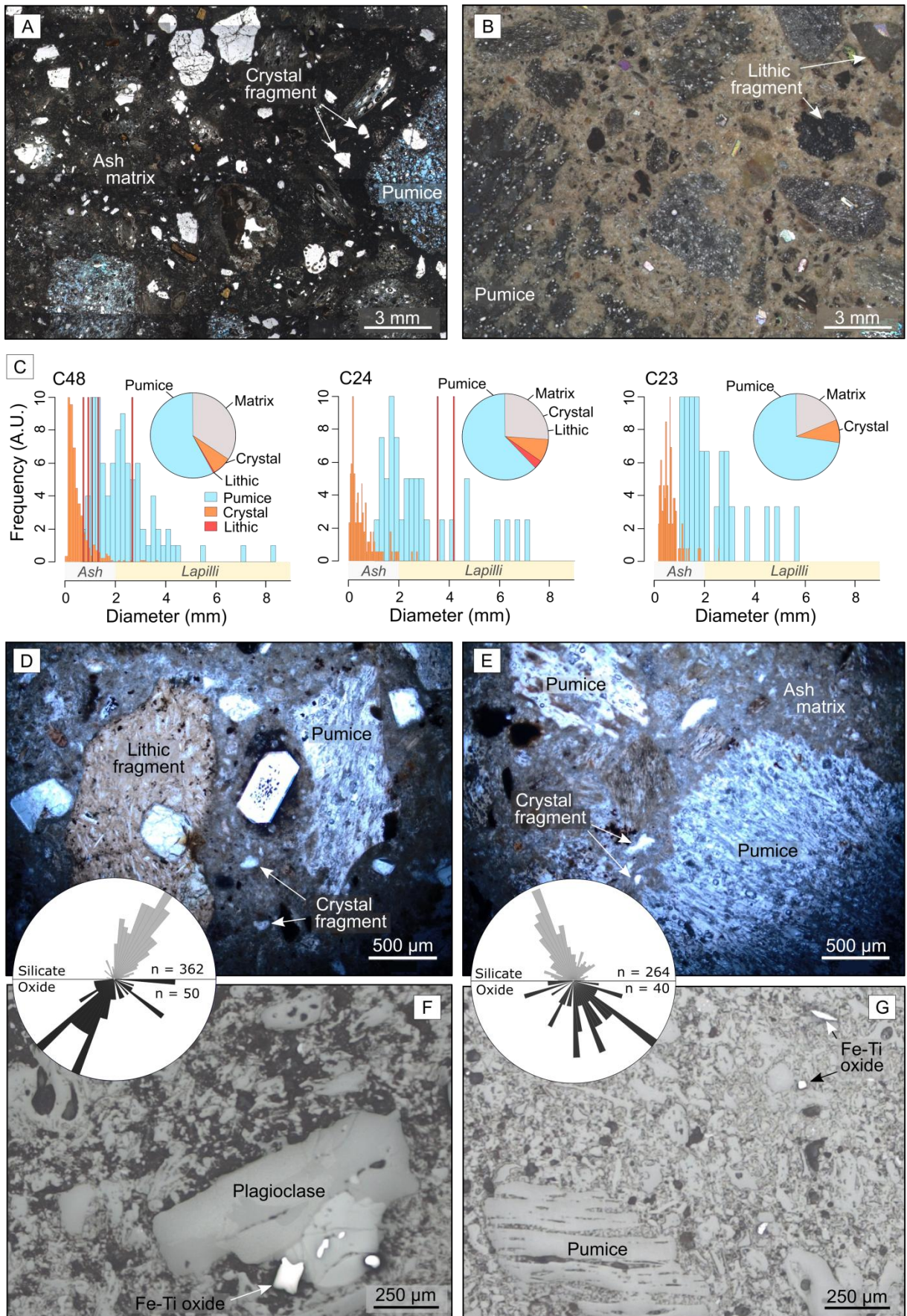
322 Quartz and feldspar dominate as the main crystal fragments, which are marked by
323 sharp and irregular shapes (Fig. 3A, B, D, E). Volcanic rocks (basaltic to basaltic-andesite in
324 composition) predominate as the main lithic clasts, typically unaltered, with irregular to
325 slightly rounded shapes (Fig. 3B, D). Pumice fragments are marked by irregular shapes and
326 high porosity values, without signs of welding or viscous/ductile deformation (Fig. 3A -
327 porosity in blue, D, E).

328 Reflected light microscopy reveals the presence of a small, sparse, distribution of Fe-
329 Ti oxides in RBI samples (Fig. 3F-G). These crystals commonly occur as primary crystals,
330 adjacent to the silicate fabric (Fig. 3F), or as crystal fragments disseminated in the ash matrix
331 (Fig. 3G). Fe-Ti oxides in the RBI commonly present diameters $<200\ \mu\text{m}$ and are marked by
332 small differences between their major and minor axis, defining a shape anisotropy. Using the
333 software ImageJ (Schindelin et al., 2012), we measured the orientation of the major axis of
334 both silicate and Fe-Ti oxide particles. The results indicate that major axes of both silicates
335 and oxides present similar, almost parallel orientation (rose diagrams in Fig. 3).

336

337 **Fig. 3.** Petrographic aspects of RBI. A) lapilli-tuff rich in crystals (transmitted light); B) lapilli-tuff rich in
338 pumice and lithic fragments (transmitted light); C) compositional estimates and size distribution of pumice,
339 crystal, lithic and matrix of RBI main body. D) lapilli-tuff showing volcanic lithic, pumice, and crystal fragments
340 (transmitted light); E) lapilli-tuff rich in non-welded pumice fragment and ash matrix (transmitted light); F)
341 detail of plagioclase crystal and several Fe-Ti oxides (reflected light); G) detail of ash matrix, pumice fragment,
342 and Fe-Ti oxide crystals (reflected light). Rose diagrams indicating both oxide and silicates (plagioclase crystals

343 and pumice fragments) major axis orientation;



344

345 4.2. Rock magnetism

346 Measurements of χ -T curves were carried out in one sample from each site (Table 1)
347 to assist the determination of the magnetic phases, their structure, and alteration history (e.g.,
348 Tarling and Hrouda, 1993; Hrouda, 2003). RBI samples present a variety of thermomagnetic
349 curves (Fig. 4A-C), with two main sets of transition temperatures (T). All samples are marked
350 by a high transition temperature (T₁), ranging from 472 to 580 °C (Fig. 4A, B, C). In addition
351 to the T₁, some samples present a secondary low transition temperature (T₂), ranging from
352 279 to 410 °C (Fig. 4B, C). When compared, heating and cooling cycles display minor
353 differences (Fig. 4A, B, C), with small values of the A₄₀ and A_{MAX} indices (Hrouda, 2003),
354 suggesting that the susceptibility is mostly reversible and new magnetic phases were not
355 created during the experiment.

356 Hysteresis loops commonly display a narrow hysteresis, with coercivities <24 mT
357 (Table 1) and low slopes, suggesting small contents of paramagnetic minerals (Fig. 4D). IRM
358 acquisition curves show that all samples reach saturation with fields ranging from 200 to 400
359 mT (Fig. 4E; Table 1), which indicates the dominance of low-coercivity magnetic minerals,
360 such as magnetite, maghemite, and greigite, which usually present M_s <300 mT (Dunlop and
361 Özdemir, 1997). However, several samples (Fig. 4E) are not completely saturated at 300 mT,
362 which indicates a small concentration of high-coercivity minerals such as hematite and
363 goethite. Hysteresis data, including the ratio of saturation remanence to saturation
364 magnetization (M_{rs}/M_s) and the coercivity of remanence to coercive force (H_{cr}/H_c), can be
365 used in the Day plot, a diagram that can help discriminate between single domain (SD),
366 pseudo-single domain (PSD) and multidomain (MD) particles (Day et al., 1977). This
367 differentiation is important because it can have effects on the behavior of the magnetic
368 particles (e.g., Moncinhatto et al., 2020). The RBI samples (Table 1) lie within the pseudo-
369 PSD and MD of the Day plot (Fig. 4F, Day et al., 1977).

370 UnMix processing reveals three distinct components contributing to the magnetization
371 observed in RBI samples (Fig. 4G, H, I). Overall, samples are characterized by either a single
372 component or two components (Table 1). Component 1 (B_1) is observed in all samples and
373 provides the strongest contribution to net magnetization (81,2 to 100%), with average field
374 ranges from 37.3 to 73.41 mT (Fig. 4G, H, I; Table 1). A second component (B_2) is also
375 observed in some samples, with fields ranging from 149.8 to 352.4 mT and contributions of
376 less than 18.7% to the net magnetization (Fig. 4H; Table 1). A third component (B_3) was
377 detected in only one sample (Fig. 4I; Table 1 - sample C29). B_3 displays the lowest coercivity
378 among our samples (9.3 mT), with a contribution to the net magnetization of 15.9% on
379 sample C29.

380 FORC diagrams typically display two components (Fig. 4J, K, L), where the first is
381 marked by a spread along the field distribution (B_u) axis and low coercivity (B_c) values and
382 the second is marked by B_u values centered around zero and a spread along the B_c axis. The
383 first behavior of FORC distribution is compatible with MD behavior, while the second
384 indicates the presence of samples with vortex domain structure (Roberts et al., 2000, 2017,
385 2018). Please check supplementary items 1, 2, and 3 for a full report on the magnetic
386 experiments.

387

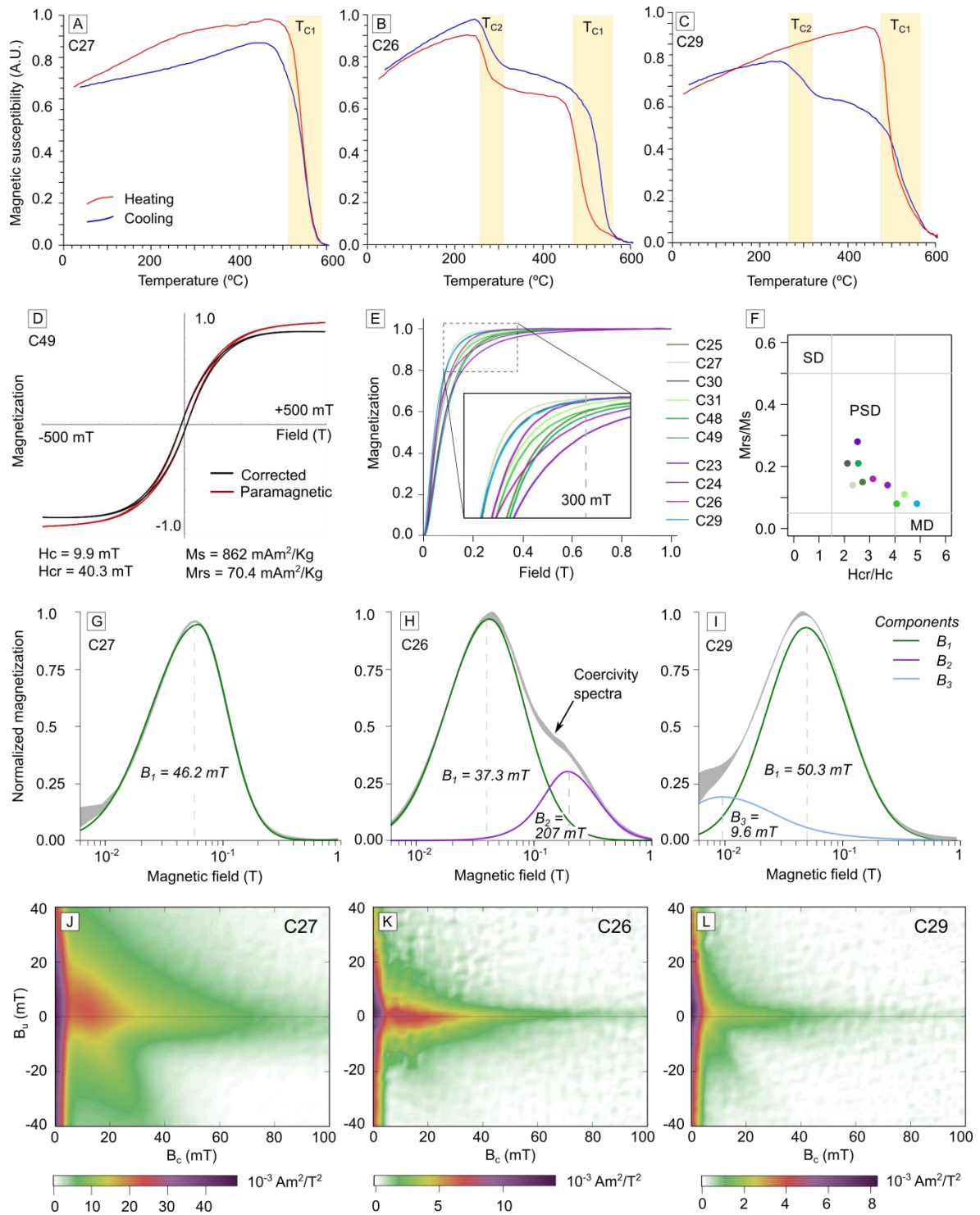
Table 1

Summary of magnetic mineralogy in RBI samples.

Unit	Site	Hysteresis and IRM results						χ -T curves	UnMix processing	FORC behavior
		M_s (mAm ² /Kg)	M_{rs} (mAm ² /Kg)	H_c (mT)	H_{cr} (mT)	H_{cr}/H_c	M_{rs}/M_s	Transitions (°C)	Components (mT)	
RB1	COP23	566.9	158.0	23.8	60.0	2.52	0.28	603	62.2 (B ₁), 352.4 (B ₂)	SV
RB2	COP24	322.2	45.1	10.9	40.4	3.71	0.14	472	42.7 (B ₁), 149.8 (B ₂)	MD
RB3	COP25	824.5	126.8	20.0	54.3	2.72	0.15	580, 410	70.1 (B ₁)	MD + SV
RB1	COP26	240.5	38.6	11.8	37.0	3.13	0.16	499, 279	37.3 (B ₁), 207.2 (B ₂)	MD + SV
RB2	COP27	1034.1	144.3	15.4	35.8	2.33	0.14	567	46.1 (B ₁)	MD
RB2	COP29	423.9	32.66	6.2	30.5	4.87	0.08	535	50.2 (B ₁), 9.63 (B ₃)	MD
RB2	COP30	420.9	86.73	17.6	37.3	2.12	0.21	537	50.5 (B ₁)	MD
RB2	COP31	411.45	43.58	8.4	36.9	4.38	0.11	573, 299	45.3 (B ₁)	MD
RB3	COP48	395.4	84.2	22.8	58.3	2.55	0.21	647, 579	73.4 (B ₁)	-
RB3	COP49	862.4	70.4	9.9	40.3	4.07	0.08	646, 577, 484	55.6 (B ₁)	-

388

Symbols: FORC states: MD = multi-domain; SV = single-vortex (Roberts et al., 2000, 2017, 2018).



389

390 **Fig. 4.** Summary of magnetic experiments: A-C) χ -T curves; D) representative hysteresis loop; E) IRM

391 curves from all sites; F) Day plot (Day et al., 1977), site colors are the same as E; G- I) representative

392 coercivity spectra and UnMix fitting; J-L) representative FORC diagrams. A.U. = Arbitrary Units.

393

Table 2*AMS results for the studied sites.*

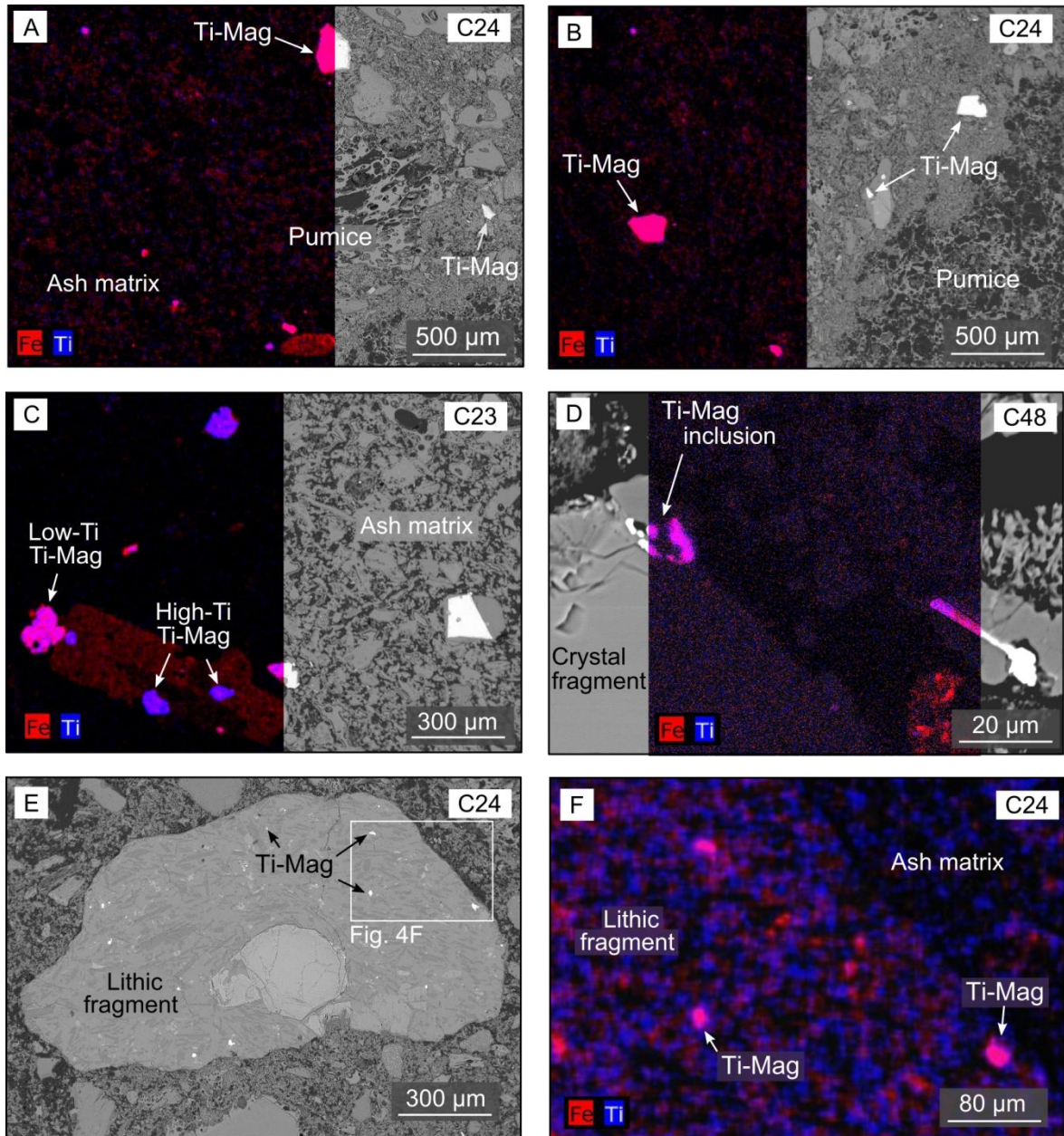
Site	UTM coordinates		Scalar results					Directional results					
	mE	mN	Km (10 ⁻³ SI)	L	F	P'	T	K ₁ D (error)	K ₁ I (error)	K ₂ D (error)	K ₂ I (error)	K ₃ D (error)	K ₃ I (error)
C23	341846	5797060	7.00	1.003	1.010	1.014	0.462	065 (25)	02 (08)	334 (25)	11 (07)	164 (09)	78 (07)
C24	341846	5797060	3.52	1.005	1.004	1.010	-0.127	337 (27)	63 (23)	186 (14)	23 (25)	091 (41)	11 (22)
C25	343248	5797194	3.25	1.010	1.019	1.031	0.328	299 (20)	19 (08)	208 (21)	02 (11)	112 (13)	70 (08)
C26	342200	5797020	2.46	1.004	1.005	1.010	0.085	310 (57)	44 (21)	216 (57)	03 (31)	123 (33)	45 (21)
C27	342191	5796983	6.50	1.005	1.006	1.012	0.125	297 (42)	28 (23)	201 (43)	11 (24)	092 (44)	59 (25)
C29	339110	5797170	4.16	1.009	1.011	1.020	0.118	312 (09)	27 (06)	221 (12)	03 (07)	124 (13)	62 (06)
C30	339107	5797178	3.41	1.003	1.004	1.007	0.188	310 (14)	17 (06)	042 (17)	07 (13)	154 (16)	71 (05)
C31	339174	5797067	2.97	1.010	1.008	1.018	-0.047	277 (33)	21 (12)	009 (32)	03 (17)	106 (33)	69 (10)
C48	344246	5794139	3.86	1.012	1.020	1.033	0.254	279 (12)	21 (21)	010 (25)	02 (10)	106 (13)	68 (11)
C49	342706	5795376	3.56	1.011	1.022	1.035	0.320	318 (17)	22 (10)	050 (21)	05 (10)	152 (16)	67 (10)

Key: number of samples (n), average magnetic susceptibility (km), lineation (L), foliation (F), degree of anisotropy (P'), shape parameter (T; [Jelinek, 1981](#)).

395 4.3. SEM observations

396 SEM observations and compositional maps obtained using EDS mapping reveal
397 titanomagnetite crystals with variable amounts of Ti as the main oxides present in RBI
398 samples (Fig. 5). These crystals occur especially as free crystals scattered in the ash matrix
399 (Fig. 5A, B, C), as well as inclusions in pumice fragments (Fig. 5B) and silicate crystals
400 (Fig. 5C, D). Minute ferromagnetic crystals are also present in the crystallographic
401 structure of silicate minerals (Fig. 5D). Lithic fragments containing embedded
402 titanomagnetite crystals are also observed (Fig. 5E, F), suggesting some contribution of
403 non-primary magnetic phases to the observed magnetization and possible nature of the
404 AMS signal.

405 The observed titanomagnetite grains display a wide variation in grain size,
406 distribution, and shape, with a predominance of irregular crystals with diameters ranging
407 from ~10 to 200 μm (Fig. 5). EDS spectra and compositional mapping reveal a
408 predominance of low-Ti titanomagnetite (Ti contents ranging from 9 to 18%), although a
409 second population of high-Ti titanomagnetite (Ti contents up to 50%) is also observed in a
410 few samples (Fig. 5C, sample C23).



411

412 **Fig. 5.** SEM observations of RBI, compositional maps (dark color), and backscattered images (greyscale
 413 images). A) titanomagnetite crystals (~200 μm) scattered in the ash matrix; B) titanomagnetite crystals (~100
 414 μm) embedded in pumice fragment; C) titanomagnetite crystals with two distinct Ti contents and sizes (~50
 415 to 150 μm) as inclusion in the silicate fabrics (left) and free crystals (right); D) minute titanomagnetite
 416 crystals (~10 μm) as inclusions in the crystallographic structure of silicate minerals; E) lithic fragment of
 417 andesitic compositions with several embedded Fe-Ti oxides; F) zoom in Fig. 5E, revealing disperse
 418 titanomagnetite crystals in the lithic fragment.

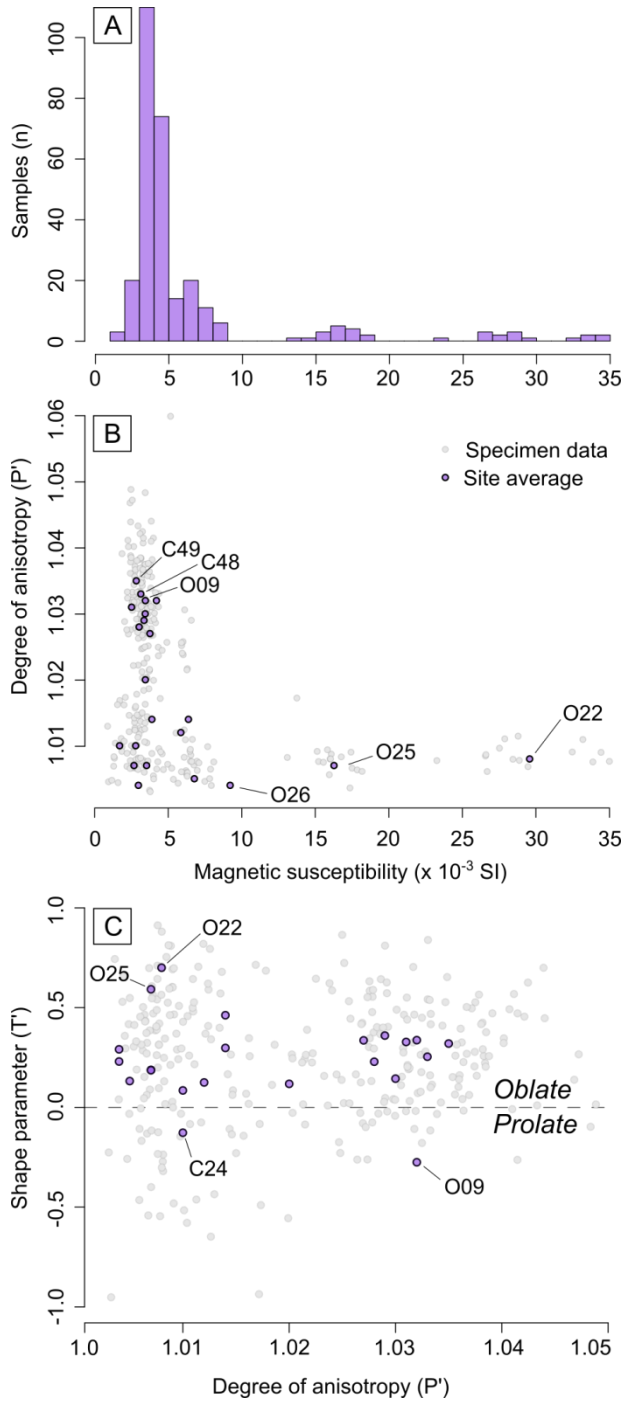
419

420

421 *4.4. AMS and structural data*

422 A total of 144 specimens were analyzed, in addition to the 145 specimens
423 previously analyzed by Ort et al (2014), representing a total of 23 AMS sites (total of 289
424 specimens). A summary of both scalar and directional data is presented in Table 2. RBI
425 samples present a low mean magnetic susceptibility (K_m), with most values clustering
426 below 10×10^{-3} SI (Fig. 6A). Notably, some sites from Ort et al. (2014) present high K_m
427 values (Fig. 6A, sites O22, 25, and 26), which is associated with the increased welding
428 degree of these sites on the mesa east of Caviahue caldera.

429 Samples present a low degree of anisotropy (P'), with typical values ranging from
430 1.003 to 1.05 (Fig. 6B). The higher P' values are observed in samples C48, C49, and O09,
431 notable sites with low K_m values and variable T parameters (Fig. 6B, Table 2). The shape
432 parameter (T) of magnetic tensors indicates a predominance of oblate ellipsoids, although
433 some samples may fall within the prolate and triaxial fields (Fig. 6C). Only two sites
434 present prolate tensors (Fig. 6C, C24, and O09).



435

436 **Fig. 6.** Summary of AMS scalar results: A) distribution of the bulk magnetic susceptibility; B) degree of
 437 anisotropy and the bulk magnetic susceptibility; C) shape parameter and degree of anisotropy.

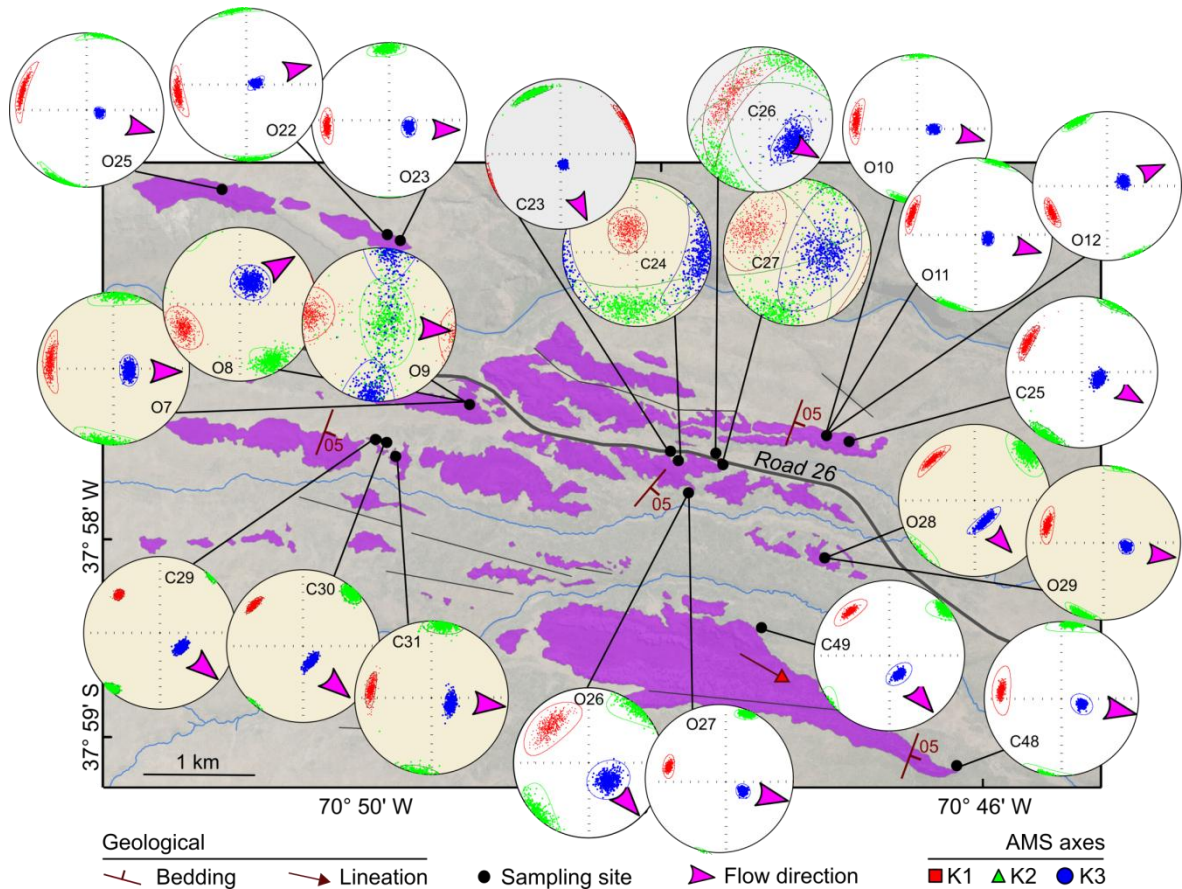
438

439 In order to assist the structural analysis, the AMS directional data were plotted in a

440 detailed map along with representative geological structures (Fig. 7). The magnetic axes

441 within each AMS site are typically well grouped (with the exception of sites C24 and C27

442 in Fig. 7), allowing AMS-based interpretations (Table 2). In most sites, the K_3 presents a
 443 general east to southeast plunge, and the magnetic lineation (K_1) is parallel to this
 444 direction, with a few exceptions (e.g., site C23, C24, C26, C27, and O09 in Fig. 7). In
 445 several sites, both K_1 (magnetic lineation) and K_2 tend to clusters (e.g., C26 and O26),
 446 suggesting the presence of oblate ellipsoids, with a well-defined K_3 (pole of the magnetic
 447 foliation).



449 **Fig. 7.** Geological map of RBI, obtained bootstrapped AMS results, and inferred flow directions.

450

451 5. Discussion

452 To identify the source area and volcanological processes associated with the RBI,
 453 we integrate fieldwork, AMS, and detailed magnetic mineralogy investigations. In the
 454 following sections, we discuss the origin of the magnetic anisotropy, the emplacement
 455 dynamics and source area of RBI, and its implications for the CCVC evolution. Finally, we

456 compare our results with available AMS data from pyroclastic sequences, addressing some
457 of the questions related to PDC dynamics and emplacement.

458

459 *5.1. Origin of the magnetic petrofabrics*

460 Recent studies have shown that AMS fabric of pyroclastic materials is strongly
461 dependent on microscopic factors, such as composition, mineral magnetic interactions, and
462 domain structure of the Fe-Ti oxides (e.g., [Cañón-Tapia and Mendoza-Borunda, 2014](#);
463 [Moncinhatto et al., 2020](#)). The AMS in pyroclastic deposits results from four main sources
464 ([Cañón-Tapia and Mendoza-Borunda, 2014](#)): (1) ferromagnetic phases (mainly Fe-Ti
465 oxides) present as free crystals, (2) ferromagnetic crystals embedded in the ash matrix,
466 pumice, clasts or shards, (3) paramagnetic minerals and (4) ferromagnetic phases as
467 inclusions on the crystallographic structure of ferrosilicate crystals. Our samples present
468 K_m values in the range of 10^{-3} SI, and according to [Tarling and Hrouda \(1993\)](#) K_m values
469 $>10^{-2}$ SI imply an AMS dominated by the ferromagnetic phases, while $K_m < 10^{-4}$ SI suggest
470 an AMS dominated by paramagnetic minerals. The theoretical contribution of
471 paramagnetic minerals to K_m (K_{PARA}) can be estimated using the geochemical composition
472 of RBI and the equations of [Syono \(1960\)](#) and [Rochette et al. \(1992\)](#):

$$473 \quad K_{PARA} = -14.6 + d (25.2 \text{ Fe}^{+2} + 33.4 \text{ Fe}^{+3} + 33.8 \text{ Mn}^{+2}) \text{ in } 10^{-6} \text{ SI}$$

474 where d is the density of rock (assumed 2.3 g/cm^3) and Fe^{+2} , Fe^{+3} , and Mn^{+2} are atomic
475 weight percent. For the estimate, we used 16 whole-rock geochemical analyses available in
476 the literature ([Mazzoni and Licitra, 2000](#); [Varekamp et al., 2006](#)). On average, K_{PARA}
477 ranges from 2×10^{-10} to 1.4×10^{-9} SI, revealing an insignificant paramagnetic contribution
478 to K_m and suggesting a main ferromagnetic origin for the AMS in our samples.

479 Petrographic analyses indicate the existence of shape anisotropy in the Fe-Ti
480 oxides. These crystals occur mainly as sparse, inequant crystals in the ash matrix ([Fig. 3](#)).

481 Directional analysis reveals that both silicate and Fe-Ti oxides present similar orientation
482 (Fig. 3, rose diagrams), indicating an effective orientation of both magnetic and silicate
483 fabrics (Archanjo and Launeau, 2004; Bascou et al., 2005). Considering the sparse
484 occurrence of Fe-Ti oxides and absence of clusters, the effects of distribution anisotropy
485 (i.e., the anisotropy resulting from clusters of magnetic particles; Hargraves et al., 1991)
486 seems to be negligible in our samples. In this context, the resulting magnetic fabrics in RBI
487 are dominated by the shape anisotropy of the ferromagnetic phases (Cañón-Tapia, 2001).

488 Thermomagnetic curves indicate the presence of three magnetic phases: low-Ti
489 titanomagnetite (T_1 , Lattard et al., 2006), high-Ti titanomagnetite, and possibly maghemite
490 (T_2 , e.g., Dedzo et al., 2011; Lattard et al., 2006). While T_1 is observed in all samples, T_2 is
491 observed in only half of our dataset. These observations are confirmed by both hysteresis
492 and IRM curves, which point to the predominance of soft magnetic phases with low H_c
493 values grouped in three distinct coercivity components: B_1 ($H_c = 37,3$ to $73,41$ mT),
494 compatible with magnetite, B_2 ($H_c = 149,8$ to $352,4$ mT), compatible with hematite and B_3
495 ($H_c = 9.3$ mT) compatible with magnetite with larger grain-size when compared to B_1 or
496 maghemite (Roberts et al., 1995; Dunlop and Özdemir, 2015).

497 In all cases, titanomagnetite grains were the dominant phase detected in SEM
498 observations, suggesting a minor contribution of secondary magnetic phases (i.e.,
499 maghemite). As a consequence, the variable presence and proportion of coercivity
500 components may be associated with lithological heterogeneities observed in the RBI, as the
501 Fe-Ti oxides embedded in lithic fragments revealed by SEM observations (Fig. 5E, F).
502 Based on the uniform magnetic mineralogy of the studied samples, changes in the AMS
503 fabrics of RBI are linked to flow dynamics.

504

505

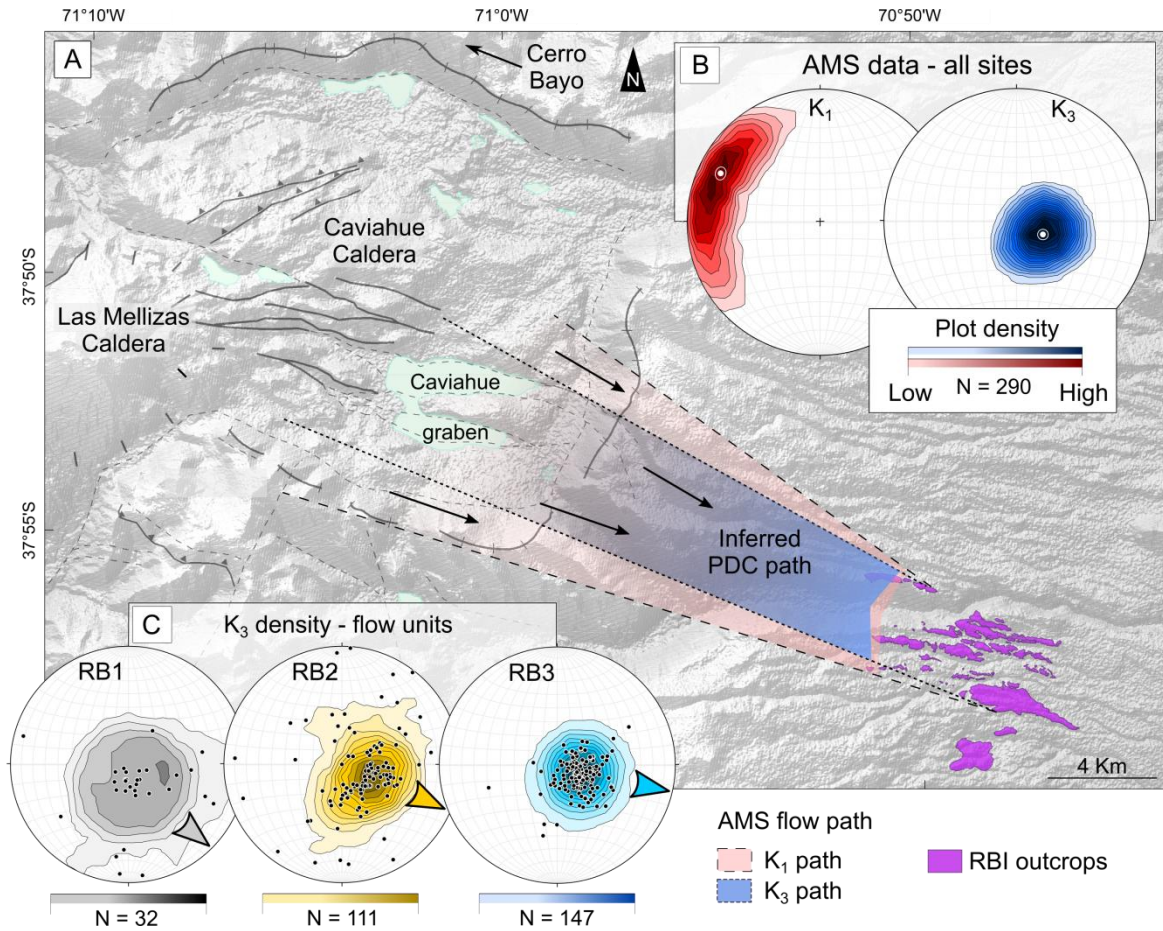
506 5.2. *Flow dynamics and emission area*

507 The predominance of imbricated oblate fabrics in our samples suggests a
508 sedimentary-related fabric as the main fabric recorded in the RBI, resulting from the
509 deposition and alignment of inequant ferromagnetic particles in the PDC (Cañón-Tapia and
510 Mendoza-Borunda, 2014). Similar to granular flow in sedimentary systems, the K_1 in
511 sedimentary fabrics of PDCs is imbricated and parallel to the flow direction (e.g., Ort,
512 1993; Cañón-Tapia and Mendoza-Borunda, 2014; Alva-Valdivia et al., 2017). In contrast,
513 the development of shear and post-emplacment fabrics (e.g., slumping, compaction)
514 seems absent in our samples, because the sampled RBI units are predominantly non-
515 welded (Mazzoni and Licitra, 2000; Melnick et al., 2006) and present emplacement
516 temperature below the minimum welding temperature (Haag et al., 2020).

517 At a site scale, AMS ellipsoids are generally well defined (Fig. 7, Table 2), with
518 well-grouped axes and consistent ESE K_3 imbrication, suggesting nearly stable deposition
519 dynamics (Cañón-Tapia and Mendoza-Borunda, 2014). In contrast, a few sites present
520 large confidence ellipses and dispersion (e.g., sites C24, 26, 27, and O09 in Fig. 7), which
521 may be linked to either poorly defined AMS tensors (low P') or unsteady depositional
522 dynamics (Cañón-Tapia and Mendoza-Borunda, 2014).

523 When considering a more regional scale (up to a few hundred meters), AMS sites
524 reveal slight variations in the PDC direction. This is highlighted by several groups of
525 proximal sites (e.g., group C30, 31 and group O7, 8, 9) that, despite having sites located
526 just a few meters from each other, present significant directional deviations (up to 33° in K_1
527 direction in group O7, 8, 9) in the resulting AMS tensor (Fig. 7). Despite these deviations,
528 a general trend in K_1 and K_3 is observed across all RBI samples and flow units (Fig. 8).

529



530

531

532 **Fig. 8.** Reconstruction of the PDC paths and potential source areas. A) Map of the CCVC with possible PDC
 533 paths based on both K_3 (blue) and K_1 (red) AMS measurements; source areas for RBI (in purple) include the
 534 Caviahue Caldera, Las Mellizas Caldera (yellow), and Cerro Bayo dome (dark red); B) stereonets with
 535 density plots for all K_1 and K_3 measurements; C) stereonets with density plots of K_3 measurements for each
 536 RBI flow unit.

537

538

539

540

541

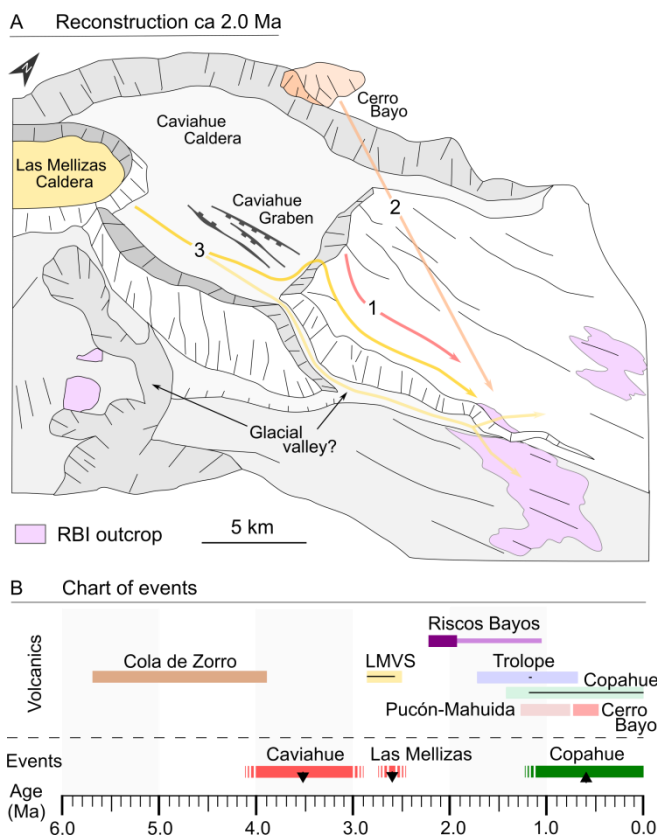
542

543

Directional statistics of the main AMS axes (Fig. 8, upper right stereograms) reveal a mean K_1 trend of 292° ($\alpha_{95} = 5.4^\circ$), while K_3 presents an average trend of 116° ($\alpha_{95} = 3.0^\circ$). AMS directional results can be used to constrain possible PDC paths, considering the α_{95} as limits for the path (Fig. 8, α_{95} of K_1 in red and α_{95} of K_3 in blue). This approach indicates an emission center located in the southern segment of the Caviahue Caldera (Fig. 8). In this segment, the most prominent emission center is the Las Mellizas Caldera (Pesce, 1989; Melnick et al., 2006).

544 *5.3. Volcanological and tectonic implications for CCVC evolution*

545 In the past decades, several source areas were proposed for RBI ignimbrites in the
 546 literature, including: (1) the Caviahue Caldera (15 x 20 km depression in Fig. 8; Mazzoni
 547 and Licitra, 2000), (2) the Las Mellizas Caldera (Fig. 8; Pesce, 1989; Melnick et al., 2006),
 548 and (3) small dome bodies located around the Caviahue Caldera (Fig. 8; Varekamp et al.,
 549 2006). Many of these models were based mainly on field, geomorphological and
 550 geochemical data. Despite significant advances in the understanding of the CCVC
 551 evolution, these studies fail to locate the emission center of the RBI. Figure 9A depicts a
 552 synthesis of the proposed emissions center and Figure 9B a chart with the main geological
 553 events and volcanic deposits in the CCVC in the last 6 Ma.



554 **Fig. 9.** Proposed source areas for RBI and main events: A) Reconstruction at ~2.0 Ma with possible PDC
 555 paths indicated by arrows: (1) Caviahue Caldera, (2) Cerro Bayo dome, and (3) Las Mellizas Caldera; B)
 556 chart of events based on the available absolute ages (Muñoz & Stern, 1988; Linares et al., 1999) and
 557 magnetic stratigraphy (Moncinhatto et al., 2019).
 558

559 One possible emission center for the RBI is the collapse of the Caviahue Caldera
560 (Mazzoni and Licitra, 2000; Ort et al., 2014). In the sampling area the RBI radiates from
561 the Caviahue Caldera (Fig. 9, red arrow number 1) and, as proposed by Ort et al. (2014),
562 RBI volume could account for at least some of the collapse of the 15 x 20 Caviahue
563 Caldera. However, the contrasting ages of the RBI and the onset of the Caviahue
564 depression suggest that these events are most likely unrelated (Fig. 9B; Linares et al.,
565 1999). Furthermore, a recent study by Hernando et al. (2020) in sediments of the Caviahue
566 Graben suggests that Caviahue Caldera was already present prior to the emplacement of
567 the ~ 2.6 Ma LMVS.

568 Additional, small emissions centers have also been mentioned, including
569 subvolcanic bodies such as Cerro Bayo, located to the north of the Caviahue Caldera (Fig.
570 9A, orange dome). However, contrasting geochemistry (Varekamp et al., 2006) and our
571 AMS data (Fig. 9A, orange arrow number 2) do not support Cerro Bayo as a potential
572 emission center.

573 Alternatively, another proposed emission center is the Las Mellizas Caldera,
574 originally located to the west of the Caviahue Caldera (Fig. 9A, yellow depression; Pesce,
575 1989; Melnick et al., 2006). Despite contrasting compositions, samples from LMVS and
576 the RBI present smooth trends in most MgO versus major elements plots, as well as
577 compatible REE patterns (Varekamp et al., 2006). In this configuration, Las Mellizas
578 comprises a nested caldera (Pesce, 1989). This setting implies that PDCs originating from
579 Las Mellizas would have to either (i) surpass the ~500-m-high east wall of the Caviahue
580 Caldera or (ii) follow a canyon to be deposited in the RBI current location (Fig. 9A, upper
581 yellow arrow number 3).

582 PDCs commonly follow the general topography and especially paleovalleys (e.g.,
583 LaBerge et al., 2006; Lesti et al., 2011; Platzman et al., 2020). In this context, the canyon

584 located in the southeastern Caviahue Caldera rim could offer a path to PDCs originated
585 from the Las Mellizas Volcano collapse (Fig. 9A, lower yellow arrow number 3).
586 However, our AMS data obtained at the end of this glacial valley do not support the lateral
587 spreading of the PDC, and instead, show a rather coherent transport direction to the east-
588 southeast (Fig. 7).

589 In contrast, field data and numerical simulations have shown that PDCs are capable
590 of overrunning topographic obstacles, even in distal regions (Legros and Kelfoun, 2000;
591 Todesco et al., 2006). The study of Todesco et al. (2006) indicates overrun of ~ 160 m
592 height obstacles and suggests that topographic barriers may induce even more collapse of
593 the eruptive column, enhancing PDC propagation. This study also indicates retention of
594 lithic clasts at the topographic barrier followed by the deposition of more pumice-rich
595 ignimbrites downcurrent. Legros and Kelfoun (2000) indicate the scaling of topographic
596 barriers as high as 1500 m for Taupo pyroclastic flows. In the field, the RBI is marked by
597 the abundance of ash and pumice fragments (which can add up to > 95%), with restricted
598 lithic-rich horizons and a massive structure, consistent with internal organization obtained
599 in the simulations of Todesco et al. (2006). The current height of the east Caviahue
600 Caldera wall is ~ 500 m. This height likely does not represent the original barrier climbed
601 by the PDCs, as the intense glaciations and magmatism in the study region probably
602 increased this collapse since the eruption of the RBI.

603 In summary, directional AMS and field data support the southern region of the
604 Caviahue Caldera as the emission center for RBI, likely the Las Mellizas Caldera. This
605 tectonic setting of multiple, nested emission centers and calderas is common in the Andes
606 (e.g., Ort et al., 1993; Chiodi et al., 2019). Despite that, we cannot rule out the possibility
607 of alternative emission areas located both inside and outside the Caviahue Caldera. These
608 virtual emission centers include the Caviahue Graben (Fig. 9A) and volcanic domes

609 originally present where the southern canyon is now located. However, geological data do
610 not indicate the presence of conduits, dikes, necks, or subvolcanic bodies in these regions
611 that could have acted as emission centers for the RBI. The AMS data show clearly that the
612 PDCs exited the Caviahue Caldera at the southeast corner and traveled downvalley from
613 there.

614

615 *5.4. Implications for PDC dynamics*

616 In the past decades the AMS has been extensively applied to pyroclastic deposits,
617 mainly as a tool for source area identification (e.g., [Palmer and MacDonald, 1999](#); [Hong et al., 2006](#);
618 [Alva-Valdivia et al., 2017](#)). Despite that, few studies have examined how AMS
619 relates to flow dynamics (e.g., [Fisher et al., 1993](#); [Baer et al. 1997](#); [Ort et al., 2003, 2014](#);
620 [Giordano et al., 2008](#); [LaBerge et al., 2009](#)). In many explosive deposits, the heterogeneity
621 of magnetic fabrics can lead to distinct interpretations, hampering the understanding of
622 questions related to flow dynamics and emplacement of PDCs (e.g., [Moncinhatto et al., 2020](#);
623 [Gambeta et al., 2021](#)). The nearly homogeneous magnetic mineralogy of RBI offers
624 the opportunity to explore these questions.

625 Several AMS studies show that, for non-welded pyroclastic sequences, the
626 magnetic foliation is commonly imbricated, with both K_1 and K_3 parallel to flow direction
627 (e.g., [Fisher et al., 1993](#); [Ort et al., 2003](#); [Giordano et al., 2008](#); [Cañón-Tapia & Mendoza-Borunda, 2014](#);
628 [Ort et al., 2014](#)). This orientation comprises the ‘parallel’ magnetic fabric
629 observed in most pyroclastic deposits ([Agrò et al., 2014](#)). However, many cases display a
630 complex behavior (e.g., [LaBerge et al., 2009](#); [Agrò et al., 2014](#); [Alva-Valdivia et al., 2017](#)),
631 expressed through ‘oblique’, ‘transverse’, and ‘random’ fabrics. In these cases,
632 interpreting AMS results and extracting flow direction pose a challenge (e.g., [LaBerge et al., 2009](#);
633 [Alva-Valdivia et al., 2017](#)). Deviations from the parallel AMS fabrics in PDCs

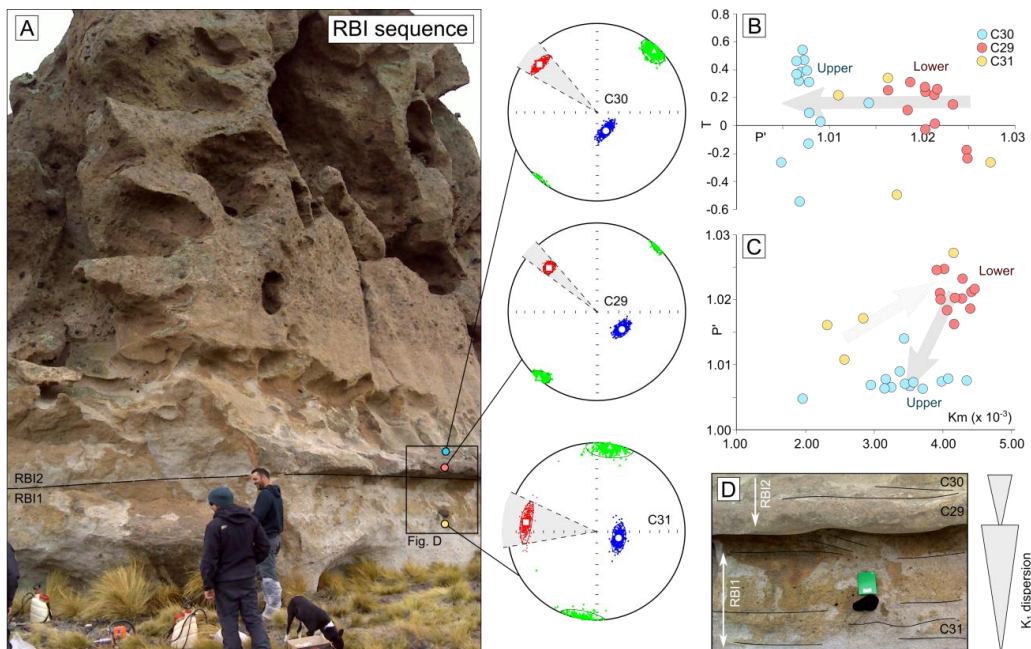
634 have been attributed to several causes, including flow dynamics (Ort et al., 1999; LaBerge
635 et al., 2009; Agrò et al., 2014; Ort et al., 2014, 2015), and mineralogy (e.g., Rochette et al.,
636 1992; Moncinhatto et al., 2020).

637 In PDCs, the flow dynamics play a significant role in the distribution and
638 orientation of magnetic particles (Ort et al., 1999, 2014, 2015; Giordano et al., 2008).
639 Following this reasoning, several studies have associated the orientation of AMS axes with
640 distance from the vent and associated PDC dynamics (e.g., Fisher et al., 1993; Baer et al.,
641 1997; Ort et al., 1999, 2003, 2015; Porreca et al., 2003). In these studies, proximal sites
642 show overlapping, dispersed, or random K_1 and K_2 axes, while more distal portions tend to
643 result in well-defined axes, with K_1 parallel to flow direction (Ort et al., 2014). In addition
644 to that, in proximal regions, the orientation of K_1 may also be orthogonal to flow direction,
645 suggesting particle rolling and the development of a transverse AMS fabric (Ort et al.,
646 1999; Agrò et al., 2014). In the RBI, only a single site displays K_1 perpendicular to flow
647 (C23), configuring a transverse fabric (Ort et al., 1999; Agrò et al., 2014). This site is
648 located in the intermediate section of the RBI and as a consequence, our samples do not
649 replicate a K_1 orientation that is dependent on the distance from the vent.

650 In contrast to the distance-dependent model, LaBerge et al. (2009) argue that
651 scattering in AMS fabrics results from the gradual decrease in transport capacity of the
652 PDC with time and changes in particle size. In this model, the upper section of a given
653 flow unit tends to present more scatter K_1 and K_3 axes (LaBerge et al., 2009). This pattern
654 in the magnetic fabric of increasing scatter up-section in PDC deposits has been reported
655 only in the welded ignimbrites of the Monte Cimino volcanic center (Italy; LaBerge et al.,
656 2009). Here we document one of the first occurrences of this effect in non-welded PDC
657 deposits.

658 In RBI sites C29, C30, and C31, AMS axis K_1 becomes progressively less
 659 constrained toward the top of each flow unit (Fig. 10A). This process also results in
 660 changes in the degree of anisotropy (Fig. 10B, C), while the basal section tends to show
 661 higher P' values, suggesting a more effective alignment of the magnetic particles (Fig.
 662 10B). Particles still present the same shape (T), size and similar K_m values. In this model,
 663 changes of P' and scattering of K_1 reflect changes in flow dynamics associated with a
 664 decrease in PDC transport capacity.

665



666

667 **Fig. 10.** Evolution of AMS fabrics and dispersion through RBI section: A) RBI flow units with stereonets; B)
 668 shape parameter and degree of anisotropy plot; C) degree of anisotropy and magnetic susceptibility plot; D)
 669 detail of the pyroclastic section and contact between upper and lower units.

670

671 [Báez et al. \(2020b\)](#) explore the pulsating behavior of PDCs at Campo de la Piedra
 672 Pómez ignimbrite (southern Puna), mainly based on extensive field data and facies
 673 analysis. The authors suggest three eruption phases marked by waxing and waning of the
 674 PDC. In the case of homogeneous, non-welded ignimbrites, such behavior may only be

675 detectable through the use of alternative fabric techniques such as the AMS. The results in
676 RBI samples suggest a stratified behavior of PDCs, which may be present even in massive
677 ignimbrites, such as the studied sequences. The origin of this behavior is associated with
678 pulsatory mechanisms of explosive eruptions (Giordano et al., 2008; Báez et al., 2020b),
679 which explain the distinctive flow units recorded in the RBI.

680

681

682 **6. Conclusions**

683 We determined the source area and emplacement dynamics of the RBI using
684 fieldwork, AMS, and magnetic mineralogy experiments. The main results for the RBI, the
685 CCVC, and emplacement of PDCs are:

- 686 1. The main carriers of the AMS in the RBI are titanomagnetite grains with low Ti
687 content. The titanomagnetite occurs as sparse, primary crystals in the ash matrix.
- 688 2. AMS fabrics in RBI are predominantly oblate with K_3 imbricated and K_1 parallel to
689 flow direction, reflecting dynamics associated with sedimentary PDC fabrics.
- 690 3. All three flow units of RBI (RB1, RB2, and RB3) present similar flow directions,
691 with a PDC path consistent with the Las Mellizas Caldera as the emission center.
- 692 4. Despite its massive nature, AMS fabrics in the RBI reveal a decrease in transport
693 capacity toward the top of each flow unit.
- 694 5. Loss of transport capacity results in an increase of AMS scattering and a decrease
695 of the degree of anisotropy (P').

696

697 **Acknowledgments**

698 This article is part of M.B.H. Master's dissertation at Geosciences Institute at
699 Universidade Federal do Rio Grande do Sul, sponsored by the Conselho Nacional de

700 Desenvolvimento Científico e Tecnológico of Brazil [grants number 400724/2014-6,
701 441766/2014-5, 304036/2018-8, 406925/2018-6, 425728/2018-8, 312737/2020-3] and
702 CAPES AUXPE [2043/2014]. The authors thank all the staff from the Paleomagnetism
703 Laboratory of Universidade de São Paulo (USPMag). We thank Léo A. Hartmann for
704 constructive comments on the manuscript. Finally, we thank Editor Heidy Mader for
705 processing the manuscript, as well as the reviewers for their valuable comments on our
706 study.

707

708 **References**

709 Agrò, A., Zanella, E., Le Pennec, J.-L., Temel, A., 2014. Magnetic fabric of ignimbrites: a
710 case study from the Central Anatolian Volcanic Province. Geological Society, London,
711 Special Publications 396, 159–175. <https://doi.org/10.1144/sp396.9>

712 Alva-Valdivia, L.M., Agarwal, A., Caballero-Miranda, C., García-Amador, B.I., Morales-
713 Barrera, W., Rodríguez-Elizarraráz, S., Rodríguez-Trejo, A., 2017. Paleomagnetic and
714 AMS studies of the El Castillo ignimbrite, central-east Mexico: Source and rock magnetic
715 nature. Journal of Volcanology and Geothermal Research 336, 140–154.
716 <https://doi.org/10.1016/j.jvolgeores.2017.02.014>

717 Archanjo, C.J., Launeau, P., 2004. Magma flow inferred from preferred orientations of
718 plagioclase of the Rio Ceará-Mirim dyke swarm (NE Brazil) and its AMS significance.
719 Geological Society, London, Special Publications 238, 285–298.
720 <https://doi.org/10.1144/gsl.sp.2004.238.01.17>

721 Baer, E.M., Fisher, R.V., Fuller, M., Valentine, G., 1997. Turbulent transport and
722 deposition of the Ito pyroclastic flow: Determinations using anisotropy of magnetic
723 susceptibility. J. Geophys. Res. 102, 22565–22586. <https://doi.org/10.1029/96jb01277>

- 724 Báez, A.D., Báez, W., Caselli, A.T., Martini, M.A., Sommer, C.A., 2020a. The
725 glaciovolcanic evolution of the Copahue volcano, Andean Southern Volcanic Zone,
726 Argentina-Chile. *Journal of Volcanology and Geothermal Research* 106866.
727 <https://doi.org/10.1016/j.jvolgeores.2020.106866>
- 728 Báez, W., de Silva, S., Chiodi, A., Bustos, E., Giordano, G., Arnosio, M., Suzaño, N.,
729 Viramonte, J.G., Norini, G., Gropelli, G., 2020b. Pulsating flow dynamics of sustained,
730 forced pyroclastic density currents: insights from a facies analysis of the Campo de la
731 Piedra Pómez ignimbrite, southern Puna, Argentina. *Bull Volcanol* 82.
732 <https://doi.org/10.1007/s00445-020-01385-5>
- 733 Barcelona, H., Yagupsky, D., Agosto, M., 2019. The layered model of the Copahue
734 geothermal reservoir, Argentina. *Geotherm Energy* 7. [https://doi.org/10.1186/s40517-019-](https://doi.org/10.1186/s40517-019-0124-9)
735 [0124-9](https://doi.org/10.1186/s40517-019-0124-9)
- 736 Bascou, J., Camps, P., Marie Dautria, J., 2005. Magnetic versus crystallographic fabrics in
737 a basaltic lava flow. *Journal of Volcanology and Geothermal Research* 145, 119–135.
738 <https://doi.org/10.1016/j.jvolgeores.2005.01.007>
- 739 Benites, S., Sommer, C.A., Lima, E.F.D., Savian, J.F., Haag, M.B., Moncinhatto, T.R.,
740 Trindade, R.I.F.D., 2020. Characterization of volcanic structures associated to the silicic
741 magmatism of the Paraná-Etendeka Province, in the Aparados da Serra region, southern
742 Brazil. *An. Acad. Bras. Ciênc.* 92. <https://doi.org/10.1590/0001-3765202020180981>
- 743 Cañón-Tapia, E., 2001. Factors affecting the relative importance of shape and distribution
744 anisotropy in rocks: theory and experiments. *Tectonophysics* 340, 117–131.
745 [https://doi.org/10.1016/s0040-1951\(01\)00150-0](https://doi.org/10.1016/s0040-1951(01)00150-0)

- 746 Cañón-Tapia, E., Mendoza-Borunda, R., 2014. Magnetic petrofabric of igneous rocks:
747 Lessons from pyroclastic density current deposits and obsidians. *Journal of Volcanology*
748 and *Geothermal Research* 289, 151–169. <https://doi.org/10.1016/j.jvolgeores.2014.11.006>
- 749 Cañón-Tapia, E., Walker, G.P.L., Herrero-Bervera, E., 1997. The internal structure of lava
750 flows—insights from AMS measurements II: Hawaiian pahoehoe, toothpaste lava and
751 “a”ā. *Journal of Volcanology and Geothermal Research* 76, 19–46.
752 [https://doi.org/10.1016/s0377-0273\(96\)00073-x](https://doi.org/10.1016/s0377-0273(96)00073-x)
- 753 Cas, R.A.F., Wright, H.M.N., Folkes, C.B., Lesti, C., Porreca, M., Giordano, G.,
754 Viramonte, J.G., 2011. The flow dynamics of an extremely large volume pyroclastic flow,
755 the 2.08-Ma Cerro Galán Ignimbrite, NW Argentina, and comparison with other flow
756 types. *Bulletin of Volcanology* 73, 1583–1609. <https://doi.org/10.1007/s00445-011-0564-y>
- 757 Cas, R.A.F., Wright, J.V., 1987. *Volcanic Successions Modern and Ancient*. Springer
758 Netherlands. <https://doi.org/10.1007/978-94-009-3167-1>
- 759 Caselli, A.T., Liccioli, C., Tassi, F., 2016. Risk Assessment and Mitigation at Copahue
760 Volcano, in: *Active Volcanoes of the World*. Springer Berlin Heidelberg, pp. 239–254.
761 https://doi.org/10.1007/978-3-662-48005-2_10
- 762 Chiodi, A., Tassi, F., Báez, W., Filipovich, R., Bustos, E., Glok Galli, M., Suzaño, N.,
763 Ahumada, Ma.F., Viramonte, J.G., Giordano, G., Pecoraino, G., Vaselli, O., 2019.
764 Preliminary conceptual model of the Cerro Blanco caldera-hosted geothermal system
765 (Southern Puna, Argentina): Inferences from geochemical investigations. *Journal of South*
766 *American Earth Sciences* 94, 102213. <https://doi.org/10.1016/j.jsames.2019.102213>
- 767 Constable, C., Tauxe, L., 1990. The bootstrap for magnetic susceptibility tensors. *J.*
768 *Geophys. Res.* 95, 8383. <https://doi.org/10.1029/jb095ib06p08383>

- 769 Day, R., Fuller, M., Schmidt, V.A., 1977. Hysteresis properties of titanomagnetites: Grain-
770 size and compositional dependence. *Physics of the Earth and Planetary Interiors* 13, 260–
771 267. [https://doi.org/10.1016/0031-9201\(77\)90108-x](https://doi.org/10.1016/0031-9201(77)90108-x)
- 772 Dedzo, M.G., Nédélec, A., Nono, A., Njanko, T., Font, E., Kamgang, P., Njonfang, E.,
773 Launeau, P., 2011. Magnetic fabrics of the Miocene ignimbrites from West-Cameroon:
774 Implications for pyroclastic flow source and sedimentation. *Journal of Volcanology and*
775 *Geothermal Research* 203, 113–132. <https://doi.org/10.1016/j.jvolgeores.2011.04.012>
- 776 de Silva, S.L., 1989. Altiplano-Puna volcanic complex of the central Andes. *Geol* 17, 1102.
777 [https://doi.org/10.1130/0091-7613\(1989\)017<1102:apvcot>2.3.co;2](https://doi.org/10.1130/0091-7613(1989)017<1102:apvcot>2.3.co;2)
- 778 Díaz, E.F.G. 2003. El englazamiento en la región de Cavihue-Copahue: su
779 reinterpretación. *Revista de la Asociación Geológica Argentina*, 58(3): 356- 366.
- 780 Dunlop, D. J., Özdemir, Ö., 1997. *Rock Magnetism*. Cambridge University Press.
781 <https://doi.org/10.1017/cbo9780511612794>
- 782 Dunlop, D.J., Özdemir, Ö., 2015. Magnetizations in Rocks and Minerals, in: *Treatise on*
783 *Geophysics*. Elsevier, pp. 255–308. <https://doi.org/10.1016/b978-0-444-53802-4.00102-0>
- 784 Ferrari, L., López-Martínez, M., Rosas-Elguera, J., 2002. Ignimbrite flare-up and
785 deformation in the southern Sierra Madre Occidental, western Mexico: Implications for the
786 late subduction history of the Farallon plate. *Tectonics* 21, 17-1-17–24.
787 <https://doi.org/10.1029/2001tc001302>
- 788 Fisher, R.V., Orsi, G., Ort, M., Heiken, G., 1993. Mobility of a large-volume pyroclastic
789 flow — emplacement of the Campanian ignimbrite, Italy. *Journal of Volcanology and*
790 *Geothermal Research* 56, 205–220. [https://doi.org/10.1016/0377-0273\(93\)90017-1](https://doi.org/10.1016/0377-0273(93)90017-1)

- 791 Folguera, A., Rojas Vera, E., Vélez, L., Tobal, J., Orts, D., Agosto, M., Caselli, A., Ramos,
792 V.A., 2016. A Review of the Geology, Structural Controls, and Tectonic Setting of
793 Copahue Volcano, Southern Volcanic Zone, Andes, Argentina, in: Active Volcanoes of the
794 World. Springer Berlin Heidelberg, pp. 3–22. [https://doi.org/10.1007/978-3-662-48005-](https://doi.org/10.1007/978-3-662-48005-2_1)
795 [2_1](https://doi.org/10.1007/978-3-662-48005-2_1)
- 796 Gambeta, J.H., Savian, J.F., Sommer, C.A., Trindade, R.I.F., 2021. Magnetic anisotropy of
797 an ancient volcanic system: Flow dynamics of post-collisional Ediacaran volcanism in
798 southernmost Brazil. *Precambrian Research* 359, 106209.
799 <https://doi.org/10.1016/j.precamres.2021.106209>
- 800 Giordano, G., Porreca, M., Musacchio, P., Mattei, M., 2008. The Holocene Secche di
801 Lazzaro phreatomagmatic succession (Stromboli, Italy): evidence of pyroclastic density
802 current origin deduced by facies analysis and AMS flow directions. *Bull Volcanol* 70,
803 1221–1236. <https://doi.org/10.1007/s00445-008-0198-x>
- 804 Graham, J. W. 1954. Magnetic susceptibility anisotropy, an unexploited petrofabric
805 element. *Geol. Soc. Am. Bull.* 65, 1257–1258.
- 806 Haag, M., Moncinhatto, T., Sommer, C., Savian, J., Caselli, A., Trindade, R., Hartmann,
807 G., Poletti, W. 2020. Source area and emplacement conditions of Riscos Bayos
808 Ignimbrites, Caviahue-Copahue Volcanic Complex (Argentina). EGU General Assembly
809 2020. <https://doi.org/10.5194/egusphere-egu2020-2704>
- 810 Haag, M.B., de Freitas, R.B., Sommer, C.A., Savian, J.F., Lima, E.F., Gambeta, J.H., Lyra,
811 D. da S., Trindade, R.I.F. da, 2021. Multi-proxy case study of a Neoproterozoic rhyolite
812 flow in southernmost Brazil: Emplacement mechanisms and implications for ancient felsic

- 813 lavas. *Journal of South American Earth Sciences* 107, 102982.
814 <https://doi.org/10.1016/j.jsames.2020.102982>
- 815 Hargraves, R.B., Johnson, D., Chan, C.Y., 1991. Distribution anisotropy: The cause of
816 AMS in igneous rocks? *Geophys. Res. Lett.* 18, 2193–2196.
817 <https://doi.org/10.1029/91gl01777>
- 818 Harrison, R.J., Feinberg, J.M., 2008. FORCinel: An improved algorithm for calculating
819 first-order reversal curve distributions using locally weighted regression smoothing.
820 *Geochem. Geophys. Geosyst.* 9, <https://doi.org/10.1029/2008gc001987>
- 821 Hernando, I.R., Bucher, J., del Papa, C.E., Eisermann, J.O., Göllner, P.L., Guzmán, S.R.,
822 Balbis, C., Petrinovic, I.A., 2020. Unraveling the timing of the Cavihue depression,
823 Andean Southern Volcanic Zone: insights from the sedimentary infill. *Int J Earth Sci (Geol*
824 *Rundsch)*. <https://doi.org/10.1007/s00531-020-01936-3>
- 825 Heslop, D., Dekkers, M.J., Kruiver, P.P., Van Oorschot, I.H.M., 2002. Analysis of
826 isothermal remanent magnetization acquisition curves using the expectation-maximization
827 algorithm. *Geophysical Journal International* 148, 58–64. [https://doi.org/10.1046/j.0956-](https://doi.org/10.1046/j.0956-540x.2001.01558.x)
828 [540x.2001.01558.x](https://doi.org/10.1046/j.0956-540x.2001.01558.x)
- 829 Hildreth, W., Moorbath, S., 1988. Crustal contributions to arc magmatism in the Andes of
830 Central Chile. *Contr. Mineral. and Petrol.* 98, 455–489.
831 <https://doi.org/10.1007/bf00372365>
- 832 Hong, H., Yu, Y., Doh, S.-J., Suk, D., Kim, J., 2016. Magnetic Fabrics and Source
833 Implications of Chisulryoung Ignimbrites, South Korea. *Front. Earth Sci.* 4.
834 <https://doi.org/10.3389/feart.2016.00079>

- 835 Hrouda, F., 1982. Magnetic anisotropy of rocks and its application in geology and
836 geophysics. *Geophysical Surveys* 5, 37–82. <https://doi.org/10.1007/bf01450244>
- 837 Hrouda, F., 2003. *Studia Geophysica et Geodaetica* 47, 847–861.
838 <https://doi.org/10.1023/a:1026398920172>
- 839 Jelinek, V., 1981. Characterization of the magnetic fabric of rocks. *Tectonophysics* 79,
840 T63–T67. [https://doi.org/10.1016/0040-1951\(81\)90110-4](https://doi.org/10.1016/0040-1951(81)90110-4)
- 841 Kruiver, P.P., Passier, H.F., 2001. Coercivity analysis of magnetic phases in sapropel S1
842 related to variations in redox conditions, including an investigation of the Sratio. *Geochem.*
843 *Geophys. Geosyst.* 2. <https://doi.org/10.1029/2001gc000181>
- 844 LaBerge, R.D., Porreca, M., Mattei, M., Giordano, G., Cas, R.A.F., 2009. Meandering flow
845 of a pyroclastic density current documented by the anisotropy of magnetic susceptibility
846 (AMS) in the quartz latite ignimbrite of the Pleistocene Monte Cimino volcanic centre
847 (central Italy). *Tectonophysics* 466, 64–78. <https://doi.org/10.1016/j.tecto.2008.09.009>
- 848 Lattard, D., Engelmann, R., Kontny, A., Sauerzapf, U., 2006. Curie temperatures of
849 synthetic titanomagnetites in the Fe-Ti-O system: Effects of composition, crystal
850 chemistry, and thermomagnetic methods. *J. Geophys. Res.* 111,
851 <https://doi.org/10.1029/2006jb004591>
- 852 Legros, F., Kelfoun, K., 2000. On the ability of pyroclastic flows to scale topographic
853 obstacles. *Journal of Volcanology and Geothermal Research* 98, 235–241.
854 [https://doi.org/10.1016/s0377-0273\(99\)00184-5](https://doi.org/10.1016/s0377-0273(99)00184-5)
- 855 Lesti, C., Porreca, M., Giordano, G., Mattei, M., Cas, R.A.F., Wright, H.M.N., Folkes,
856 C.B., Viramonte, J., 2011. High-temperature emplacement of the Cerro Galán and

- 857 Toconquis Group ignimbrites (Puna plateau, NW Argentina) determined by TRM analyses.
858 Bull Volcanol 73, 1535–1565. <https://doi.org/10.1007/s00445-011-0536-2>
- 859 Linares, E., Ostera, H.A. & Mas, L., 1999. Cronologia potasio-argon del complejo efusivo
860 Copahue-Caviahue, Provincia del Neuquen, Rev. Asoc. Geol. Argentina, 54(3), 240–247.
- 861 Magee, C., Stevenson, C., O’Driscoll, B., Schofield, N., McDermott, K., 2012. An
862 alternative emplacement model for the classic Ardnamurchan cone sheet swarm, NW
863 Scotland, involving lateral magma supply via regional dykes. Journal of Structural
864 Geology 43, 73–91. <https://doi.org/10.1016/j.jsg.2012.08.004>
- 865 Maxbauer, D.P., Feinberg, J.M., Fox, D.L., 2016. MAX UnMix: A web application for
866 unmixing magnetic coercivity distributions. Computers & Geosciences 95, 140–145.
867 <https://doi.org/10.1016/j.cageo.2016.07.009>
- 868 Mazzoni, M.M., Licitra, D. 2000. Significado estratigráfico y volcanológico de ignimbritas
869 neógenas con composición intermedia en la zona del lago Caviahue, Neuquén. Revista de
870 la Asociación Geológica Argentina, 55 (3): 188–200.
- 871 Melnick, D., Folguera, A., Ramos, V.A., 2006. Structural control on arc volcanism: The
872 Caviahue–Copahue complex, Central to Patagonian Andes transition (38°S). Journal of
873 South American Earth Sciences 22, 66–88. <https://doi.org/10.1016/j.jsames.2006.08.008>
- 874 Moncinhatto, T. R., Oliveira, W.P., Haag, M. B., Hartmann, G.A., Savian, J. F., Poletti,
875 W., Sommer, C.A., Caselli, A.T., Trindade, R.I.F., 2019. Paleosecular variaton from
876 Northern Patagonia recorded by 0-5 Ma Caviahue-Copahue lava flows. In: Sixth Biennial
877 Meeting of Latinmag, Rancagua. Latinmag Letters. Rancagua,. v. 9. p. 1-7.

- 878 Moncinhatto, T.R., Haag, M.B., Hartmann, G.A., Savian, J.F., Poletti, W., Sommer, C.A.,
879 Caselli, A.T., Trindade, R.I.F., 2020. Mineralogical control on the magnetic anisotropy of
880 lavas and ignimbrites: a case study in the Caviahue-Copahue field (Argentina).
881 Geophysical Journal International 220, 821–838. <https://doi.org/10.1093/gji/ggz483>
- 882 Morgan, L.A., Doherty, D.J., Leeman, W.P., 1984. Ignimbrites of the Eastern Snake River
883 Plain: Evidence for major caldera-forming eruptions. J. Geophys. Res. 89, 8665.
884 <https://doi.org/10.1029/jb089ib10p08665>
- 885 Muñoz, J.B., and Stern, C.R., 1988, The Quaternary volcanic belt of the southern
886 continental margin of South America: Transverse structural and petrochemical variations
887 across the segment between 38S and 39S: Journal of South American Earth Sciences, v. 1,
888 no. 2, p. 147–161. [https://doi.org/10.1016/0895-9811\(88\)90032-6](https://doi.org/10.1016/0895-9811(88)90032-6)
- 889 Ort, M.H., 1993. Eruptive processes and caldera formation in a nested downsagcollapse
890 caldera: Cerro Panizos, central Andes Mountains. Journal of Volcanology and Geothermal
891 Research 56, 221–252. [https://doi.org/10.1016/0377-0273\(93\)90018-m](https://doi.org/10.1016/0377-0273(93)90018-m)
- 892 Ort, M.H., Rosi, M., Anderson, C.D., 1999. Correlation of deposits and vent locations of
893 the proximal Campanian Ignimbrite deposits, Campi Flegrei, Italy, based on natural
894 remanent magnetization and anisotropy of magnetic susceptibility characteristics. Journal
895 of Volcanology and Geothermal Research 91, 167–178. [https://doi.org/10.1016/s0377-
896 0273\(99\)00034-7](https://doi.org/10.1016/s0377-0273(99)00034-7)
- 897 Ort, M.H., Newkirk, T.T., Vilas, J.F., Vazquez, J.A., 2014. Towards the definition of AMS
898 facies in the deposits of pyroclastic density currents. Geological Society, London, Special
899 Publications 396, 205–226. <https://doi.org/10.1144/sp396.8>

- 900 Ort, M.H., Orsi, G., Pappalardo, L., Fisher, R.V., 2003. Anisotropy of magnetic
901 susceptibility studies of depositional processes in the Campanian Ignimbrite, Italy. *Bulletin*
902 *of Volcanology* 65, 55–72. <https://doi.org/10.1007/s00445-002-0241-2>
- 903 Ort, M.H., Porreca, M., Geissman, J.W., 2015. The use of palaeomagnetism and rock
904 magnetism to understand volcanic processes: introduction. Geological Society, London,
905 *Special Publications* 396, 1–11. <https://doi.org/10.1144/sp396.17>
- 906 Palmer, H.C., MacDonald, W.D., 1999. Anisotropy of magnetic susceptibility in relation to
907 source vents of ignimbrites: empirical observations. *Tectonophysics* 307, 207–218.
908 [https://doi.org/10.1016/s0040-1951\(99\)00126-2](https://doi.org/10.1016/s0040-1951(99)00126-2)
- 909 Pasqualon, N.G., Savian, J.F., Lima, E.F., Luz, F.R, Moncinhatto, T.R., Trindade, R.I.F,
910 2020. Emplacement dynamics of alkaline volcanic and subvolcanic rocks in Trindade
911 Island, Brazil. *Journal of Volcanology and Geothermal Research* 406, 107078.
912 <https://doi.org/10.1016/j.jvolgeores.2020.107078>
- 913 Pesce, A. 1989. Evolución volcano-tectónica del complejo efusivo Copahue– Caviahue y
914 su modelo geotérmico preliminar. *Revista de la Asociación Geológica Argentina*, 44: 307–
915 327
- 916 Platzman, E.S., Sparks, R.S.J., Cooper, F.J., 2020. Fabrics, facies, and flow through a
917 large-volume ignimbrite: Pampa De Oxaya, Chile. *Bull Volcanol* 82.
918 <https://doi.org/10.1007/s00445-019-1345-2>
- 919 Porreca, M., Mattei, M., Giordano, G., De Rita, D., Funicello, R., 2003. Magnetic fabric
920 and implications for pyroclastic flow and lahar emplacement, Albano maar, Italy. *J.*
921 *Geophys. Res.* 108. <https://doi.org/10.1029/2002jb002102>

- 922 Pueyo Anchuela, Ó., Gil Imaz, A., Gil-Peña, I., Maestro, A., Galindo-Zaldivar, J., López-
923 Martínez, J., Rey, J., Soto, R., Oliva-Urcia, B., 2014. Application of AMS for
924 reconstruction of the geological evolution of recent volcanic systems: Case of Deception
925 Island (South Shetland Islands, Antarctica). *Tectonophysics* 626, 69–85.
926 <https://doi.org/10.1016/j.tecto.2014.03.032>
- 927 Roberts, A.P., Almeida, T.P., Church, N.S., Harrison, R.J., Heslop, D., Li, Y., Li, J.,
928 Muxworthy, A.R., Williams, W., Zhao, X., 2017. Resolving the Origin of Pseudo-Single
929 Domain Magnetic Behavior. *J. Geophys. Res. Solid Earth* 122, 9534–9558.
930 <https://doi.org/10.1002/2017jb014860>
- 931 Roberts, A.P., Cui, Y., Verosub, K.L., 1995. Wasp-waisted hysteresis loops: Mineral
932 magnetic characteristics and discrimination of components in mixed magnetic systems. *J.*
933 *Geophys. Res.* 100, 17909–17924. <https://doi.org/10.1029/95jb00672>
- 934 Roberts, A.P., Pike, C.R., Verosub, K.L., 2000. First-order reversal curve diagrams: A new
935 tool for characterizing the magnetic properties of natural samples. *J. Geophys. Res.* 105,
936 28461–28475. <https://doi.org/10.1029/2000jb900326>
- 937 Roberts, A.P., Tauxe, L., Heslop, D., Zhao, X., Jiang, Z., 2018. A Critical Appraisal of the
938 “Day” Diagram. *J. Geophys. Res. Solid Earth* 123, 2618–2644.
939 <https://doi.org/10.1002/2017jb015247>
- 940 Robertson, D.J., France, D.E., 1994. Discrimination of remanence-carrying minerals in
941 mixtures, using isothermal remanent magnetization acquisition curves. *Phys. Earth planet.*
942 *Inter.* 82, 223–234.

- 943 Rochette, P., Jackson, M., Aubourg, C., 1992. Rock magnetism and the interpretation of
944 anisotropy of magnetic susceptibility. *Rev. Geophys.* 30, 209.
945 <https://doi.org/10.1029/92rg00733>
- 946 Schindelin, J., Arganda-Carreras, I., Frise, E., Kaynig, V., Longair, M., Pietzsch, T.,
947 Preibisch, S., Rueden, C., Saalfeld, S., Schmid, B., Tinevez, J.-Y., White, D.J., Hartenstein,
948 V., Eliceiri, K., Tomancak, P., Cardona, A., 2012. Fiji: an open-source platform for
949 biological-image analysis. *Nat Methods* 9, 676–682. <https://doi.org/10.1038/nmeth.2019>
- 950 Sielfeld, G., Cembrano, J., Lara, L., 2017. Transtension driving volcano-edifice anatomy:
951 Insights from Andean transverse-to-the-orogen tectonic domains. *Quaternary International*
952 438, 33–49. <https://doi.org/10.1016/j.quaint.2016.01.002>
- 953 Sommer, C. A., Haag, M. B., Caselli, A. T. 2016. Determinação numérica de parâmetros
954 reológicos para sistemas vulcânicos de diferentes composições e idades. In: X Simpósio
955 Sul-Brasileiro de Geologia, Curitiba. Boletim de Resumos do X Simpósio Sul-Brasileiro de
956 Geologia. Curitiba: SBG/UFPR, 2017. v. 10.
- 957 Sparks, R.S.J., 1976. Grain size variations in ignimbrites and implications for the transport
958 of pyroclastic flows. *Sedimentology* 23, 147–188. [https://doi.org/10.1111/j.1365-
959 3091.1976.tb00045.x](https://doi.org/10.1111/j.1365-3091.1976.tb00045.x)
- 960 Stern, C.R., 2004. Active Andean volcanism: its geologic and tectonic setting. *Revista*
961 *geológica de Chile* 31. <https://doi.org/10.4067/s0716-02082004000200001>
- 962 Syono, Y., 1960. Magnetic Susceptibility of Some Rock Forming Silicate Minerals Such as
963 Amphiboles, Biotites, Cordierites and Garnets. *J. geomagn. geoelec* 11, 85–93.
964 <https://doi.org/10.5636/jgg.11.85>

- 965 Tarling, D. H., Hrouda, F., 1993. The Magnetic Anisotropy of Rocks. London: Chapman &
966 Hall, 217p. <https://doi.org/10.1002/gj.3350300111>
- 967 Tassi, F., Vaselli, O., Caselli, A.T. (Eds.), 2016. Copahue Volcano, Active Volcanoes of
968 the World. Springer Berlin Heidelberg. <https://doi.org/10.1007/978-3-662-48005-2>
- 969 Tauxe, L., Banerjee, S.K., Butler, R.F., Van Der Voo R., 2018. Essentials of
970 Paleomagnetism, 5th Web Edition
- 971 Tauxe, L., Kylstra, N., Constable, C., 1991. Bootstrap statistics for paleomagnetic data.
972 Journal of Geophysical Research 96, 11723. <https://doi.org/10.1029/91jb00572>
- 973 Todesco, M., Neri, A., Esposti Ongaro, T., Papale, P., Rosi, M., 2006. Pyroclastic flow
974 dynamics and hazard in a caldera setting: Application to Phlegrean Fields (Italy).
975 Geochem. Geophys. Geosyst. 7, n/a-n/a. <https://doi.org/10.1029/2006gc001314>
- 976 Trolese, M., Cerminara, M., Esposti Ongaro, T., Giordano, G., 2019. The footprint of
977 column collapse regimes on pyroclastic flow temperatures and plume heights. Nature
978 Communications 10. <https://doi.org/10.1038/s41467-019-10337-3>
- 979 Varekamp, J.C., deMoor, J.M., Merrill, M.D., Colvin, A.S., Goss, A.R., Vroon, P.Z.,
980 Hilton, D.R., 2006. Geochemistry and isotopic characteristics of the Caviahue-Copahue
981 volcanic complex, Province of Neuquén, Argentina, in: Evolution of an Andean Margin: A
982 Tectonic and Magmatic View from the Andes to the Neuquén Basin (35°-39°S Lat).
983 Geological Society of America. [https://doi.org/10.1130/2006.2407\(15\)](https://doi.org/10.1130/2006.2407(15))
- 984 Velez, M.L., Euillades, P., Caselli, A., Blanco, M., Díaz, J.M., 2011. Deformation of
985 Copahue volcano: Inversion of InSAR data using a genetic algorithm. Journal of

986 Volcanology and Geothermal Research 202, 117–126.

987 <https://doi.org/10.1016/j.jvolgeores.2011.01.012>

988 Willcock, M.A.W., Mattei, M., Hasalová, P., Giordano, G., Cas, R.A.F., Morelli, C., 2014.

989 Flow behavior in the intra-caldera setting: an AMS study of the large (>1290 km³)

990 Permian Ora ignimbrite. Geological Society, London, Special Publications 396, 177–204.

991 <https://doi.org/10.1144/sp396.3>